PI3Kα inhibitor and degrader inavolisib can co-opt FGFR2 to enhance responses in patients with *PIK3CA*-mutated solid tumors and in preclinical models

Dejan Juric [1 #] *, Kyung Song [2] *, Radia M. Johnson [2] *, Melissa K. Accordino [3], Philippe L. Bedard [4], Andrés Cervantes [5], Valentina Gambardella [5], Erika Hamilton [6], Antoine Italiano [7, 8], Kevin Kalinsky [9], Ian E. Krop [10], Mafalda Oliveira [11], Cristina Saura [11], Peter Schmid [12], Nicholas C. Turner [13], Andrea Varga [14], Steven Gendreau [15], Michael S. Hwang [15], Zheng Kuang [15, 16], Jeffery T. Lau [17], Eva Lin [18], Trang Pham [2], Danilo Maddalo [17], Matthew G. Rees [19], Melissa M. Ronan [19], Jennifer A. Roth [19], Scott Martin [18], Nicole M. Sodir [17], Ethan S. Sokol [15, 16], Zachary J. Whitfield [20], Alice Wong [21], Robert L. Yauch [2], Junko Aimi [15], Sravanthi Cheeti [22], Jill Fredrickson [23], Stephanie Hilz [15], Marc Hafner [2, 24], Katherine E. Hutchinson [15], Yanling Jin [25], Ubong Peters [26], Daniel Zingg [2], Stephanie Royer-Joo [26], Noopur Shankar [27], Jennifer L. Schutzman [26], Komal L. Jhaveri [28 #], Anwesha Dey [2 #]

Affiliations:

[1] Mass General Cancer Center, Department of Medicine, Harvard Medical School, Boston, MA.

[2] Genentech, Department of Discovery Oncology, South San Francisco, CA.

[3] Columbia University Medical Center, Division of Hematology and Oncology, Department of Medicine, Columbia University, New York, NY.

[4] Division of Medical Oncology & Hematology, Princess Margaret Cancer Centre, Department of Medicine, University of Toronto, Toronto, Canada.

[5] Medical Oncology Dept. Hospital Clinico Universitario. INCLIVA, Biomedical Research Institute. University of Valencia, Valencia, Spain.

[6] Sarah Cannon Research Institute, Nashville, TN.

[7] Institut Bergonie, Early Phase Trials and Sarcoma Units, Bordeaux, France.

[8] University of Bordeaux, Bordeaux, France.

[9] Winship Cancer Institute, Emory University, Atlanta, GA.

[10] Dana-Farber Cancer Institute, Harvard Medical School, Boston, MA.

[11]Medical Oncology Department, Vall d'Hebron University Hospital and Breast Cancer Group, Vall d'Hebron Institute of Oncology (VHIO), Barcelona, Spain.
[12]Centre of Experimental Medicine, Barts Cancer Institute, Queen Mary University London, London, UK.
[13]Institute of Cancer Research and Royal Marsden Hospital, London, UK.
[14]Department of Drug Development, Gustave Roussy Cancer Campus, Villejuif, France.
[15]Genentech, Department of Translational Medicine, South San Francisco, CA.
[16]Foundation Medicine Inc., Cambridge, MA.
[17]Genentech, In Vivo Pharmacology Department, South San Francisco, CA.
[18]Genentech, Molecular Discovery Cancer Cell Biology, South San Francisco, CA.
[19]The Broad Institute of MIT and Harvard, Cambridge, MA.
[20]Rancho Biosciences, San Diego, CA.
[21]Genentech, Medicinal Chemistry, South San Francisco, CA.
[22]Genentech, Developmental Science Clinical Pharmacology, South San Francisco, CA.
[23]Genentech, Clinical Imaging, South San Francisco, CA.
[24]Department of Oncology Bioinformatics, South San Francisco, CA
[25]Roche, Data Science, Mississauga, Canada.
[26]Genentech, Oncology, South San Francisco, CA.
[27]Genentech, Safety Science, South San Francisco, CA.
[28]Memorial Sloan Kettering Cancer Center, New York, NY.
* Equal contributions
[#] Co-corresponding authors

Running title:
PI3Kα inhibitor/degrader inavolisib and the FGFR2 influence

Details for co-corresponding authors:
Dejan Juric, M.D., Mass General Cancer Center, Department of Medicine, Harvard Medical School, Boston, MA. E-mail: Juric.Dejan@mgh.harvard.edu
Komal L. Jhaveri, M.D., Memorial Sloan Kettering Cancer Center, New York, NY. Email: jhaverik@mskcc.org
Anwesha Dey, Ph.D., Genentech, Inc., 1 DNA Way, South San Francisco, CA 94080, USA. E-mail: dey.anwesha@gene.com

Keywords:
PI3Kα inhibitor; FGFR2; PIK3CA; breast cancer; HR+/HER2−

Disclosures and conflict of interest in the past 36 months

	Name	
1	Alice Wong	Employee of Roche/Genentech and owns stock in Roche.
2	Andrea Varga	Employee at AstraZeneca and owns stock in AstraZeneca.
3	Andrés Cervantes	Institutional research funding from Genentech, Merck Serono, Bristol Myers Squibb, Merck Sharp & Dohme, Roche, BeiGene, Bayer, Servier, Lilly, Novartis, Takeda, Astellas, Natera, FibroGen; and advisory board or speaker fees from Amgen, Merck Serono, Roche, Bayer, Servier, Pierre Fabre.
4	Antoine Italiano	Research grant from Astra Zeneca, Bayer, BMS, Merck, MSD, Lilly, Novartis, Pharmamar, Roche; advisory board from Astra Zeneca, Bayer, BMS, Merck, MSD, Lilly, Novartic, Pharmamar, Roche.
5	Anwesha Dey	Employee of Roche/Genentech and owns stock in Roche.
6	Cristina Saura	Consulting/advisory board/travel grant from AstraZeneca, AX'Consulting, Byondis B.V, Daiichi Sankyo, Eisai, Exact Sciences, Exeter Pharma, F.Hoffmann-La Roche Ltd, Gilead, Lilly, MediTech, Merck Sharp & Dohme, Novartis, Pfizer, Philips, Pierre Fabre, PintPharma, Puma Biotechnology, SeaGen, Synthon biopharmaceutical, Zymeworks.
7	Daniel Zingg	Employee of Roche/Genentech and owns stock in Roche.
8	Danilo Maddalo	Employee of Roche/Genentech and owns stock in Roche.
9	Dejan Juric	Consulting or speaking fees from AstraZeneca, Pfizer, Eli Lilly, Eisai, Genentech/Roche, Guardant Health, Ipsen, Novartis, PIC Therapeutics, Relay Therapeutics, Syros, Vibliome, Transcode; holds equity in PIC Therapeutics, Relay Therapeutics; research funding from Arvinas, AstraZeneca, Blueprint, Eli Lilly, InventisBio, Novartis, Genentech/Roche, Pfizer, Ribon, Scorpion Therapeutics, Seagen, Takeda.
10	Erika Hamilton	Research funding to institution from Abbvie, Acerta Pharma, Accutar Biotechnology, ADC Therapeutics, AKESOBIO Australia, Amgen, Aravive, ArQule, Artios, Arvinas, AstraZeneca, AtlasMedx, BeiGene, Black Diamond, Bliss BioPharmaceuticals, Boehringer Ingelheim, Cascadian Therapeutics, Clovis, Compugen, Context Therapeutics, Cullinan, Curis, CytomX, Daiichi Sankyo, Dana Farber Cancer Inst, Dantari, Deciphera, Duality Biologics, eFFECTOR Therapeutics, Ellipses Pharma, Elucida Oncology, EMD Serono, FujiFilm, G1

		Therapeutics, H3 Biomedicine, Harpoon, Hutchinson MediPharma, Immunogen, Immunomedics, Incyte, Infinity Pharmaceuticals, InventisBio, Jacobio, Karyopharm, K-Group Beta, Kind Pharmaceuticals, Leap Therapeutics, Lilly, Loxo Oncology, Lycera, Mabspace Biosciences, Macrogenics, MedImmune, Mersana, Merus, Millennium, Molecular Templates, Novartis, Nucana, Olema, OncoMed, Onconova Therapeutics, Oncothyreon, ORIC Pharmaceuticals, Orinove, Orum Therapeutics, Pfizer, PharmaMar, Pieris Pharmaceuticals, Pionyr Immunotherapeutics, Plexxikon, Prelude Therapeutics, Profound Bio, Radius Health, Regeneron, Relay Therapeutics, Repertoire Immune Medicine, Rgenix, Roche/Genentech, SeaGen, Sermonix Pharmaceuticals, Shattuck Labs, StemCentRx, Sutro, Syndax, Syros, Taiho, TapImmune, Tesaro, Tolmar, Torque Therapeutics, Treadwell Therapeutics, Verastem, Zenith Epigenetics, Zymeworks. Consulting/advisory role – all payments to institution from AstraZeneca, Daiichi Sankyo, Ellipses Pharma, Gilead Sciences, Greenwich LifeSciences, Janssen, Jazz Pharmaceuticals, Lilly, Loxo, Medical Pharma Services, Mersana, Novartis, Olema Pharmaceuticals, Orum Therapeutics, Pfizer, Relay Therapeutics, Roche/Genentech, SeaGen, Stemline Therapeutics, Theratechnologies, Tubulis, Verascity Science, Zentalis Pharmaceuticals
11	Ethan S. Sokol	Employee at Foundation Medicine and a Shareholder in Roche
12	Eva Lin	Employee of Roche/Genentech and owns stock in Roche.
13	Ian E. Krop	Research funding/grants to institution from Genentech/Roche, Pfizer, Macrogenics; Consulting fees/advisory board/honoraria from Daiichi/Sankyo, Macrogenics, Genentech/Roche, Seagen, AstraZeneca; Data safety monitoring committee member at Novartis, Merck, Seagen; Chief Scientific Officer at Translational Breast Cancer Research Consortium.
14	Jeffery T. Lau	Employee of Roche/Genentech and owns stock in Roche.
15	Jennifer A. Roth	Employee of the Broad Institute of MIT and Harvard, Cambridge, MA.
16	Jennifer L. Schutzman	Employee of Roche/Genentech and owns stock in Roche.

17	Jill Fredrickson	Employee of Roche/Genentech and owns stock in Roche.
18	Junko Aimi	Employee of Genentech/Roche and owns stock in Roche.
19	Katherine E. Hutchinson	Employee of Roche/Genentech and owns stock in Roche.
20	Kevin Kalinsky	Spouse was an employee at EQRX previously; Consulting fees/advisory board from Genentech/Roche, Immunomedics, Seattle Genetics, Daiichi Sankyo, Puma Biotechnology, Mersana, Menarini Silicon Biosystems, Myovant Sciences, Takeda.
21	Komal L Jhaveri	Consulting or advisory role at Abbvie, AstraZeneca, Biotheranostics, BluePrint Medicines, Bristol-Myers Squibb, Daiichi Sankyo, Genentech, Intellisphere, Jounce therapeutics, Lilly, Novartis, Pfizer, Sanofi, Seagen, Sun Pharma Advanced Research Company, Synthon, Taiho Oncology; Research funding to institution from ADC Therapeutics, AstraZeneca, Clovis Oncology, Debiopharm Group, Genentech, Immunomedics, Lilly, Novartis, Novita Pharmaceuticals, Pfizer, Puma Biotechnology, VelosBio/Merck, Zymeworks; Travel, accommodations, and expenses from AstraZeneca, Intellisphere, Jounce Therapeutics, Pfizer, Taiho Pharmaceutical.
22	Kyung Song	Employee of Roche/Genentech and owns stock in Roche.
23	Mafalda Oliveira	Honoraria from Eisai Europe, Gilead Sciences, MSD, Novartis, Pfizer, Roche, SeaGen; Consulting or advisory role at AstraZeneca, Daiichi Sankyo/Astra Zeneca, Gilead Sciences, ITeos Therapeutics, Relay Therapeutics, Roche/Genentech, Seagen; Research funding to institution from AstraZeneca, Ayala Pharmaceuticals, Boehringer Ingelheim, Gilead Sciences, GlaxoSmithKline, Roche/Genentech, Seagen, Zenith Epigenetics; Travel, accommodations, expenses from AstraZeneca Spain, Eisai, Gilead Sciences, Pierre Fabre.
24	Marc Hafner	Employee of Roche/Genentech and owns stock in Roche.
25	Matthew G. Rees	Employee of the Broad Institute of MIT and Harvard, Cambridge, MA.
26	Melissa K. Accordino	None
27	Melissa M. Ronan	Employee of the Broad Institute of MIT and Harvard, Cambridge,

		MA.
28	Michael S. Hwang	Employee of Roche/Genentech and owns stock in Roche.
29	Nicholas C. Turner	Advisory board honoraria from Astra Zeneca, Lilly, Pfizer, Roche/Genentech, Novartis, GlaxoSmithKline, Repare Therapeutics, Relay Therapeutics, Zentalis, Gilead, Inivata, Guardant, Exact Sciences; Research funding from Astra Zeneca, Pfizer, Roche/Genentech, Merck Sharpe and Dohme, Guardant Health, Invitae, Inivata, Personalis, Natera.
30	Nicole M. Sodir	Employee of Roche/Genentech and owns stock in Roche.
31	Noopur Shankar	Employee of Roche/Genentech and owns stock in Roche.
32	Peter Schmid	Grants/research support to my institution from AZ, Genentech, Roche, Oncogenex, Novartis, Astellas, Medivation; consulting fees or honoraria from Pfizer, AZ, Daiichi, Novartis, Gilead, Roche, Sanofi, Merck, MSD, BI, Seagen, Amgen, Bayer, Eisai, Celgene, Lilly, Puma.
33	Philippe L. Bedard	Uncompensated advisory boards for BMS, Pfizer, SeaGen, Lilly, Amgen, Merck, Zymeworks, Gilead, Janssen; institutional research support from BMS, Sanofi, AZ, Amgen, Pfizer, Genentech/Roche, GSK, Novartis, Merck, SeaGen, Zymeworks, Lilly, Amgen, Bicara Therapeutics, Medicenna, Takeda.
34	Radia M. Johnson	Former employee of Genentech; current employee and stockholder of Gilead.
35	Robert L. Yauch	Employee of Roche/Genentech and owns stock in Roche.
36	Scott Martin	Employee of Roche/Genentech and owns stock in Roche.
37	Sravanthi Cheeti	Employee of Roche/Genentech and owns stock in Roche.
38	Stephanie Hilz	Employee of Roche/Genentech and owns stock in Roche.
39	Stephanie Royer-Joo	Employee of Roche/Genentech and owns stock in Roche.
40	Steven Gendreau	Employee of Roche/Genentech and owns stock in Roche.
41	Trang Pham	Employee of Roche/Genentech and owns stock in Roche.
42	Ubong Peters	Employee of Roche/Genentech and owns stock in Roche.

43	Valentina Gambardella	Advisory Board fees from Boehringer Ingelheim; research funding from Bayer, Boehringer, Roche; institutional funding from Genentech, Merck Serono, Roche, Beigene, Bayer, Servier, Lilly, Novartis, Takeda, Astelas, Fibrogen, Amcure, Natera, Sierra Oncology, Astra Zeneca, Medimmune, BMS, MSD.
44	Yanling Jin	Employee of Roche/Genentech and owns stock in Roche.
45	Zachary J. Whitfield	Employee of Rancho Biosciences, San Diego, CA
46	Zheng Kuang	Employee at Foundation Medicine and a Shareholder in Roche

ABSTRACT

Background: *PIK3CA* mutations frequently drive solid tumors, particularly hormone receptor-positive (HR+) breast cancer. Inavolisib, an ATP-competitive p110α inhibitor, also promotes the degradation of mutated p110α. PI3K inhibitors have generally shown modest single-agent activity and have safety concerns.

Method: A first-in-human Phase 1 study (NCT03006172) evaluated oral inavolisib in patients with *PIK3CA*-mutated solid tumors, to determine the maximum tolerated dose (MTD) and safety. Correlative analyses included circulating tumor DNA (ctDNA). Preclinical studies in cell lines and xenografts elucidated the role of FGFR2.

Results: The MTD was 9 mg daily, with a manageable safety profile (e.g., hyperglycemia, diarrhea). Inavolisib showed linear pharmacokinetics, consistent pharmacodynamic modulation, and antitumor activity in HR+ *PIK3CA*-mutated breast cancer (26% objective response rate, 45% clinical benefit rate). *FGFR2* hotspot mutations in ctDNA were strongly associated with clinical benefit. Preclinically, oncogenic FGFR2 signaling enhanced inavolisib sensitivity by engaging HER3, RAS, and p85β, that facilitated mutated p110α degradation, surpassing non-degrading inhibitors. Combination therapy with FGFR2 inhibitors showed synergy and delayed resistance.

Conclusion: These findings highlight a novel cooperativity between FGFR2 and p110α that boosts the effectiveness of inavolisib. The data support advancing precision oncology beyond single biomarkers to complex algorithms utilizing co-occurring alterations, particularly suggesting that combining inavolisib with FGFR2 inhibitors may offer enhanced and more durable responses in *PIK3CA/FGFR2*-altered tumors.

Statement of translational relevance

By linking ctDNA-identified mutations with reported clinical benefit from inavolisib, we found FGFR2 hotspot mutations may drive enhanced dependency through the PI3K pathway. The elucidated cooperativity between FGFR2 and p110α may further contribute to a shift in precision oncology paradigms from a single predictive biomarker to a more complex algorithm based on co-occurring alterations.

INTRODUCTION

Phosphoinositide 3-kinase (PI3K) is a multi-domain lipid kinase that, upon activation by integrins and growth factor receptors, regulates cell proliferation, survival, and migration through the PI3K/protein kinase B/mammalian target of rapamycin (PI3K/AKT/mTOR) signaling pathway. There are three classes of PI3K, with Class I being the most responsive to external stimuli and comprising two subunits: a regulatory adapter subunit (p85), and a catalytic subunit (p110) inclusive of four isoforms – alpha, beta, delta, and gamma. The p110 alpha isoform (p110α) and p85 subunit make up the PI3Kα complex. The *PIK3CA* gene, which encodes p110α, can be affected by oncogenic hotspot mutations present in 13% of all solid tumors (1). *PIK3CA* driver mutations are particularly pronounced in breast cancer, with 35-40% of hormone receptor-positive (HR+) and 25-30% of human epidermal growth factor receptor-2-positive (HER2+) breast cancers exhibiting *PIK3CA* mutations (2,3). More recently, tumors with two or more variants in *PIK3CA* have been identified (4-7). When occurring in *cis*, multi-mutant *PIK3CA* are associated with increased PI3K-pathway dependency, and thus, enhanced sensitivity to pharmacologic inhibition of p110α (8-10). Several PI3K inhibitors are in clinical development. Some have been discontinued due to safety concerns (11), including hyperglycemia, diarrhea and other gastrointestinal adverse events (AEs), skin toxicities, and liver toxicities (12). Moreover, PI3K inhibitors have demonstrated modest activity as single agents, prompting the investigation of combination-therapy regimens.

We previously reported that inavolisib, a potent, selective, and ATP-competitive inhibitor of p110α, promotes the degradation of mutated p110α, particularly in HER2+ breast cancer cell line models (13,14). These data suggested that receptor tyrosine kinase (RTK)-dependent

inducible degradation of mutated p110α drives sensitivity to inavolisib in HER2+ tumors (14). Herein, we report clinical results from the first-in-human Phase 1 trial of inavolisib in patients with cancers harboring one or more *PIK3CA* hotspot mutations *(PIK3CA*mut) and demonstrate that the additional presence of activating mutations in the fibroblast growth factor receptor 2 (*FGFR2*) gene in patients with HR+/HER2− advanced breast cancer is associated with clinical benefit during inavolisib monotherapy. *FGFR2* and its three paralogs *FGFR1*, *FGFR3*, and *FGFR4* encode the FGFR family of transmembrane RTKs (15). Fibroblast growth factor (FGF) ligands bind these receptors to exert their pleiotropic effects, and oncogenic FGFR signaling mediated by somatic alterations has been implicated in numerous tumor types (16-18). *FGFR2*-amplified tumors with FGFR2 overexpression promote oncogene addiction through partial crosstalk between FGFR2 and other receptors such as HER3 (19).

We demonstrate that high FGFR2 expression in cell lines is associated with FGFR2-dependence and susceptibility to inavolisib through multiple signaling nodes including human epidermal growth factor receptor-3 (HER3), rat sarcoma (RAS), and with direct binding of FGFR2 to the p85β PI3K regulatory subunit. FGFR2-activated HER3 potentiates the inavolisib degradation mechanism-of-action (MOA), leading to a stronger growth-inhibitory effect as compared to a non-degrading p110α inhibitor. In cells expressing high levels of FGFR2, inavolisib was synergistic with an FGFR2-selective inhibitor and delayed resistance to either single agent. Our findings suggest that FGFR2-dependent tumors may benefit from a combination of inavolisib and an FGFR2-selective inhibitor to further improve clinical outcomes.

METHODS

Clinical study design

This was an open-label, multicenter, multi-arm, Phase I study (ClinicalTrials.gov identifier: NCT03006172) that included a single-agent (Arm A), 3+3 dose-escalation design to evaluate the safety, tolerability, and pharmacokinetics (PK) of inavolisib (GDC-0077; RO7113755) administered orally to patients with locally advanced or metastatic *PIK3CA*mut solid tumors. The primary objective was to determine the maximum tolerated dose (MTD) and/or Recommended Phase II Dose (RP2D), and to assess the safety of inavolisib in patients with *PIK3CA*mut solid tumors. The starting dose was 6 mg, which was below the maximum recommended starting dose calculated from relevant toxicity data from preclinical studies. Patients received their first dose on Day 1 in Cycle 1 (C1D1), followed by a 7-day washout period and several PK samplings. Patients started once-daily (QD) dosing on C1D8; the first cycle was 35 days, and subsequent cycles were 28 days.

The study was conducted in full conformance with the ICH E6 guideline for Good Clinical Practice and the principles of the Declaration of Helsinki, or the applicable laws and regulations of the country in which the research was conducted, whichever afforded the greater protection to the individual. The study complied with the requirements of the ICH E2A guideline (Clinical Safety Data Management: Definitions and Standards for Expedited Reporting). The protocol was approved by institutional review boards (IRBs) at participating institutions and patients provided written informed consent prior to any study procedures.

Patients

The study enrolled male and female patients, with histologically documented and locally advanced, recurrent, or metastatic, *PIK3CA*mut, incurable solid tumor malignancy, including breast cancer. Patients presented with disease that had progressed after all available standard therapy or for which standard therapy had proven to be ineffective or intolerable, or considered inappropriate. *PIK3CA*mut tumor status was determined from Sponsor central testing of fresh or archival tumor tissue with the PCR-based cobas® *PIK3CA* Mutation Test (Roche;), or site-directed local testing of tumor tissue or plasma-derived circulating tumor DNA (ctDNA). Study-eligible mutations included H1047R/Y/L, E542K, E545K/D/G/A, Q546K/R/E/L, N345K, C420R, G1049R, R88Q, and M1043I.

Patients were ≥18 years old with evaluable or measurable disease per RECIST v1.1. They had an Eastern Cooperative Oncology Group (ECOG) performance status of 0 or 1; life expectancy of ≥12 weeks; adequate hematologic and organ function within 14 days prior to study treatment; fasting glucose ≤140 mg/dL and glycosylated hemoglobin (HbA1c) <7%; adequate liver function (bilirubin ≤1.5 × upper limit of normal (ULN), serum albumin ≥2.5 g/dL, AST and ALT ≤2.5 × ULN except patients with documented liver metastases); adequate kidney function (serum creatinine ≤1.5 × ULN or creatine clearance ≥50 mL/minute), INR <1.5 × ULN and aPTT <1.5 × ULN.

Patients were allowed to join the dose escalation cohorts (Arm A) even if they had prior treatment with a PI3K inhibitor. Exclusion criteria were the presence of metaplastic breast cancer; history of leptomeningeal disease; type 1 or 2 diabetes requiring anti-hyperglycemic medication. Other exclusion criteria were known and untreated active central nervous system

metastases; uncontrolled pleural effusion or ascites requiring recurrent drainage procedures ≥ biweekly; and some eye conditions (concurrent ocular or intraocular condition; inflammatory or infectious conditions; history of idiopathic or autoimmune-associated uveitis).

Safety

All patients who received any amount of study treatment were included in the safety analyses. Adverse events occurring on or after treatment on Day 1 were summarized by mapped term and National Cancer Institute Common Terminology Criteria for Adverse Events (NCI CTCAE) v4.0 toxicity grade.

The dose-limiting toxicity (DLT) assessment window was C1D1 to C1D35. DLT definition included fasting hyperglycemia Grade ≥4; fasting hyperglycemia Grade ≥3 lasting >7 days despite appropriate oral treatment; fasting hypercholesterolemia Grade ≥4; triglyceridemia lasting >14 days despite appropriate intervention; elevated serum hepatic transaminase (ALT or AST) Grade ≥3 lasting >7 days; elevated serum bilirubin Grade ≥3; neutropenia Grade ≥4 lasting >7 days; febrile neutropenia Grade ≥3; thrombocytopenia Grade ≥4; thrombocytopenia Grade 3 associated with clinically significant bleeding or requiring platelet transfusion in the absence of anti-coagulation therapy or a condition that presents a bleeding risk. Any non-hematologic, non-hepatic, non-metabolic AE of Grade ≥3 was also considered a DLT with the following exceptions: alopecia; vomiting or nausea Grade ≥3 with improvement to Grade ≤2 in ≤3 days with treatment; diarrhea Grade ≥3 with improvement to Grade ≤1 in ≤7 days with treatment; fatigue Grade 3 lasting ≤3 days or less than two grade changes from baseline; asymptomatic Grade 3 laboratory abnormalities. During the DLT assessment window, patients who

discontinued from the study or missed >3 doses of inavolisib were replaced in the absence of a DLT.

Pharmacokinetics

The PK evaluable population consisted of all patients who received at least one dose of the study drug and had ≥1 evaluable post-dose PK sample. PK parameters were derived from the plasma concentration-time profile of inavolisib following single-dose and multiple dose administration using Non-compartmental Analysis (NCA).

Efficacy

The best overall response rate was defined as the percentage of patients who achieved a best overall response of complete response (CR) or partial response (PR) according to RECISTv1.1. The confirmed overall response rate required consecutive assessment of PR or CR >4 weeks after the initial documentation of response. Patients missing response data were classified as non-responders. Clinical benefit rate was defined as percent of patients with confirmed CR, PR, and those with ≥24 weeks duration of stable disease (SD) or non-CR/non-progressive disease (PD) since first study treatment.

Statistical considerations

The sample size for Arm A was based on dose-escalation rules. The sample sizes did not reflect any explicit power and type I error considerations. This study was intended to obtain preliminary safety, PK, pharmacodynamics (PD), and activity information in the safety-

evaluable population. For each cohort and dose level, 95% confidence intervals (CI) were calculated for the activity endpoints. Continuous variables were summarized using means, standard deviations, median, and ranges; categorical variables were summarized using counts and percentages. Safety was assessed through summaries of adverse events, changes in laboratory test results, and changes in vital signs.

FDG-PET imaging

^{18}F-fluorodeoxyglucose positron emission tomography (FDG-PET) scans were acquired prior to treatment (baseline) and after 2 weeks of QD treatment (C1D22-28, or C1D15-22 for backfill patients). On-treatment scans were acquired 1-4 h after inavolisib dosing, with a blood glucose requirement of <180 mg/dL prior to all scans. Quantitative assessment of scans was performed centrally by one radiologist. Up to five target lesions with a tumor-to-background ratio of at least 2:1 and 15 mm in longest diameter were selected at baseline. Partial metabolic response was defined as a decrease of >25% in the mean percentage change in the maximum standardized uptake value (SUV_{max}, lean body mass corrected) of the target lesions, and no new FDG-avid lesions.

Immunohistochemical (IHC) analysis of paired tumor tissue samples

Paired formalin-fixed and paraffin-embedded (FFPE) tumor tissue samples collected from patients prior to treatment (baseline) and during treatment (C1D15) underwent immunohistochemical (IHC) analysis with antibodies against Ki67 (rabbit monoclonal antibody, clone 30-9, Ventana/Roche Diagnostics, Cat# 790-4286, RRID:AB_ 2631262), phosphorylated

AKT (Phospho-Akt [Ser473] [D9E] XP® rabbit monoclonal antibody, Cell Signaling Technology, Cat# 4060, RRID:AB_2315049), and S6 (Phospho-S6 Ribosomal Protein [Ser235/236] [D57.2.2E] XP® rabbit monoclonal antibody, Cell Signaling Technology, Cat# 4858, RRID:AB_916156). Ki67 was scored as the total percentage of cells with nuclear staining in each sample. Cytoplasmic staining of pAKT and pS6 was scored by H-score methodology, where intensity is considered "0" for absent expression, 1+ for weak staining, 2+ for moderate staining, and 3+ for strong staining, and where H-score = (percentage of cells with absent staining x 0) + (percentage of 1+ cells x 1) + (percentage of 2+ cells x 2) + (percentage of 3+ cells x 3). The percent change in each score within a patient was computed as 100x a patient's (on treatment - pre-treatment)/pre-treatment score and displayed as a barplot to illustrate the change in staining/expression for each marker and sample pair.

Analysis of blood plasma-derived circulating tumor DNA (ctDNA) from study patients

ctDNA was isolated as previously described (20) from plasma collected immediately prior to treatment (baseline) and on C1D15 of treatment from 19 study participants (C1D15 only available for 14 of these) for sequencing with the FoundationACT (FACT) comprehensive genomic profiling (CGP) assay - a laboratory developed test (LDT) predecessor to the FDA-approved FoundationOne®Liquid CDx - in a Clinical Laboratory Improvement Amendments (CLIA)-certified, College of American Pathologists (CAP)-accredited reference laboratory (Foundation Medicine, Inc., Cambridge, MA, USA). Comprehensive details on these assay platforms, sequencing, and mutation calling methodologies were previously described (20,21).

For mutation allele frequency (MAF) dynamics analyses, MAF for *PIK3CA* is defined as the percentage of mapped reads supporting the variant. For patients with >1 *PIK3CA* single nucleotide variant (SNV; includes both known pathogenic and unknown *PIK3CA* mutations), the sum of the MAFs of each SNV is used. At baseline, all patients with ctDNA available contained at least one pathogenic *PIK3CA* mutation that met enrollment criteria.

For the comprehensive analysis to understand genomic features associated with response to inavolisib, ctDNA derived from plasma samples collected at different timepoints including C1D1 (baseline, *n*=20), on treatment at C1D15 (*n*=16), and at study completion (end of treatment, *n*=15) was sequenced using the FACT or the updated and similar LDT FoundationOne®Liquid assay as described (20,21). Only samples with at least one detected alteration were included in the analysis. Cell-free DNA genomic profiling of plasma samples using the FoundationOne®Liquid assay were performed in a CLIA-certified, CAP-accredited laboratory (Foundation Medicine Inc., Cambridge, MA, USA) using hybrid-capture, adapter ligation-based libraries to identify genomic alterations (base substitutions, small insertions and deletions, copy number alterations, and rearrangements/fusion events) for 70 cancer-related genes. Processing of the sequence data and identification of different classes of genomic alterations were performed as previously described (21). Unless otherwise indicated, the analysis focused on alterations predicted to be pathogenic, defined as of known or likely oncogenic significance. Description of analysis of genomic features is described in Methods subsection "Statistical analyses for translational research."

Real-world clinical genomics database analyses

Genomic alterations (substitutions, indels, copy number alterations, and rearrangements) were identified via next generation sequencing (NGS)-based comprehensive genomic profiling (CGP) for >300 cancer-related genes (FDA-approved FoundationOne®CDx, and the LDT FoundationOne®) (21). For the analyses herein, we queried the CGP data from 49,834 breast tumors (including 2,626 ER+ breast tumors) sequenced up to June 30, 2023. The analysis of prevalence and co-occurrence of *FGFR2* and *PIK3CA* alterations was performed on the CGP data from 45,847 HER2− breast tumors and 476,781 solid tumor biopsies sequenced up to June 30, 2023.

Statistical analysis for translational research

Statistical analysis, computation, and plotting were performed using R version 4.2.0. All statistical tests were two-sided. Pairwise comparisons were corrected for multiple testing using the Benjamini & Hochberg method. Regularized Cox logistic regression was used to discover cell free DNA genomic alterations associated with clinical benefit to inavolisib. Two-way ANOVA (type III) analysis was performed on the unbalanced drug sensitivity AUC data after Box-Cox transformation in R using BoxCox function with lambda set to "auto" from the forecast R package (version 8.17.0) to satisfy the assumption of homogeneity of variances verified by Levene's test. All possible pairwise comparisons using a Bonferroni adjustment with the emmeans R package (version 1.8.3). Raw counts or normalized data were used for all other statistical tests.

Chemical reagents

Tool compounds and inhibitors were made according to known methods/procedures in the literature or acquired from commercially available sources.

Antibody reagents

Antibodies to p110α (Cat# 4249, RRID:AB_2165248), pAKT Ser473 (Cat# 4060, RRID:AB_2315049), pS6 S235/236 (Cat# 2211, RRID:AB_ 331679), HER3 (Cat# 12708, RRID:AB_2721919), HER2 (Cat# 2242, RRID:AB_331015), pHER2 Y1221/Y1222 (Cat# 2243, RRID:AB_490899), pHER3 Y128 (Cat# 4791, RRID:AB_2099709), pHER3 Y1328 (Cat# 14525, RRID:AB_2798501), pPLCγ Y783 (Cat# 14008, RRID:AB_2728690), pERK T202/T204 (Cat# 9101, RRID:AB_331646), p4EBP T37/46 (Cat# 9459, RRID:AB_330985), FGFR1 (Cat# 9740, RRID:AB_11178519), FGFR2 (Cat# 11835, RRID:AB_2797742), FGFR3 (Cat# 4574, RRID:AB_2246903), FGFR4 (Cat# 8562, RRID:AB_10891199), pFGFR Y653/654 (Cat# 3476, RRID:AB_331369), pFRS2A Y196 (Cat# 3864, RRID:AB_2106222) were obtained from Cell Signaling Technology (Danvers, MA). Antibody to β-actin (Cat# A5441, RRID:AB_476744) was from Sigma-Aldrich. Antibodies to Ras (Cat# ab52939, RRID:AB_2121042), p85α (Cat# ab133595, RRID:AB_3662733), and p85β (Cat# ab28356, RRID:AB_777259) were obtained from Abcam (Cambridge, MA). Peroxidase goat anti-rabbit IgG (Cat# 111-035-144, RRID:AB_2307391), and Peroxidase goat anti-mouse IgG (Cat# 115-035-146, RRID:AB_2307392) were obtained from Jackson ImmunoResearch (West Grove, PA). Ubiquitin reagent TUBE1 (UM101) was obtained from LifeSensors, Inc. (Malvern, PA).

PRISM assay

In brief, inavolisib was treated at 8 doses in triplicate across 900 PRISM barcoded cancer cell lines for five days (22). All cell lines were cultured in RPMI 1640 with 10% FBS. Cell lines were lysed with Qiagen TCL buffer to isolate mRNA. mRNA was then reverse-transcribed into cDNA and then the sequence containing the unique PRISM barcode was amplified using PCR. Finally, Luminex beads that recognize the specific barcode sequences were hybridized to the PCR products and then detected using a Luminex scanner, which reports signal as a median fluorescent intensity (MFI). The data was then processed to calculate AUC, IC50, and create dose response curves. The details of the data processing steps are at: https://github.com/cmap/dockerized_mts

Cell lines and cell culture

All cell lines used in this article were from the Genentech tissue culture cell line bank. (Supplementary Table S1). All cell lines underwent authentication by Short 461 Tandem Repeat (STR) profiling, single nucleotide polymorphism (SNP) fingerprinting, and mycoplasma testing. STR profiles were determined for each line using the Promega PowerPlex 16 System. This is performed once and compared to external STR profiles of cell lines (when available) to determine cell line ancestry. SNP profiles are performed each time new stocks are expanded for cryopreservation. Cell line identity is verified by high-throughput SNP profiling using Fluidigm multiplexed assays. SNPs were selected based on minor allele frequency and presence on commercial genotyping platforms. SNP profiles are compared to SNP calls from available internal and external data (when available) to determine or confirm ancestry. All stocks are

tested for mycoplasma prior to and after cells are cryopreserved. Two methods are used to avoid false positive/negative results: Lonza Mycoalert and Stratagene Mycosensor.

Cell lines (Supplementary Table S1) were cultured in RPMI media prepared by the Genentech media preparation group. Powdered RPMI (Gibco Cat# 31800-105) was mixed with distilled water, 2 g/L sodium bicarbonate (Sigma Cat# S5761-1KG) was added next, and the final volume was adjusted with distilled water. The pH was adjusted to fall within the range of 7.00 +/- 0.01. The prepared RPMI was supplemented with 10% heat-inactivated FBS (Corning Cat#35-016-cm), 2 mM Glutamax (Gibco Cat# 35050-061), and 100 U/ml Pen Strep (Gibco Cat# 15140-122). The medium was immediately processed into sterile containers by membrane filtration with a 0.2-μm filter using a positive-pressure system.

All cell lines for signaling experiments were cultured in the same growth media described above. Once we received the cells, they were expanded 2-3 times using 0.5% trypsin for dissociation, following the subculturing procedures described in Supplementary Table S1.

Viability assay CellTiter-Glo

Cells were seeded (1000-2000 cells/well) in 384-well plates for 16 h. Compounds were added to the media to each well such that the desired concentration was achieved. Cell viability was assessed by quantitating ATP using CellTiter-Glo (Promega, Madison, WI) after 5 days of incubation. After 5 days, relative numbers of viable cells were measured by luminescence using CellTiter-Glo® (Promega) according to the manufacturer's instructions and read on a Wallac Multilabel Reader (PerkinElmer, Foster City). The EC50 calculations were carried out using Prism 6.0 software (GraphPad, San Diego). GR values (23) were calculated using the gDR

package in R (24) and reference division time (23,24). All metrics are reported in Supplementary Table S2. Synergy was assessed by excess over single agent and excess over Bliss independence (25).

siRNA transfection

Transfection of siRNA was carried out using Lipofectamine RNAiMAX reagent (Thermo Fisher Scientific Cat# 13778150) 72 hours in advance of drug treatment. siRNA details are as follows:

- FGFR1 siRNA : Synthesized and chemically modified by Dharmacon Inc. ON-TARGETplus Human FGFR1 (2260) siRNA-SMARTpool cat ID: L-003131-00-0005
- FGFR2 siRNA : Synthesized and chemically modified by Dharmacon Inc. ON-TARGETplus Human FGFR2 (2263) siRNA-SMARTpool cat ID: L-003132-00-0005
- FGFR3 siRNA : Synthesized and chemically modified by Dharmacon Inc. ON-TARGETplus Human FGFR3 (2261) siRNA-SMARTpool cat ID: L-003133-00-0005
- FGFR4 siRNA : Synthesized and chemically modified by Dharmacon Inc. ON-TARGETplus Human FGFR4 (2264) siRNA-SMARTpool cat ID: L-003134-00-0005
- ERBB3 siRNA : Synthesized and chemically modified by Dharmacon Inc. ON-TARGETplus Human ERBB3 (2065) siRNA-SMARTpool cat ID: L-003127-00-0005

To generate the T47D_mutant line bearing p110a H1047R as a homozygous mutant, two CRISPR-Cas9 constructs were designed. One was designed to specifically target the WT allele in exon 21 (gRNA H1047R-2, ATGAATGATGCACATCATGG) and the second designed to target the intron of both WT and mutant alleles (gRNA H1047R-7, ACATTTGAGCAAAGACCTGA).

Plasmids for each targeting pair were cotransfected using Turbofectin (Thermofisher). After 48 hours, cells were put under selection with 1 μg/mL puromycin. Puromycin-resistant cells were further selected by collecting GFP-expressing cells by flow cytometry, and clones were expanded in standard cell culture conditions to create stable lines. Targeting efficiency of the CRISPR-induced allelic knockouts was assessed by PCR flanking the target sites (forward: TGCTGTGAAGGAAAATGGAA; reverse: TGCAGTGTGGAATCCAGAGTGAGC) and clones further validated with qRT-PCR.

RNA isolation and *PIK3CA* allele–specific qRT-PCR

Total RNA was isolated from cells using the RNeasy Plus Mini Kit (Qiagen) following manufacturer's instructions. First-strand cDNA synthesis and RT-qPCR was carried out using the One step RT QPCR reagent (Applied Biosystems). Resulting signal was detected on an Applied Biosystems Real Time PCR System. Primers and allele-specific probes were as follows:

PIK3CA H1047R-forward: GGCTTTGGAGTATTTCATGAAACA

PIK3CA H1047R-reverse: GAAGATCCAATCCATTTTTGTTGTC

PIK3CA H1047R WT-probe: ATGATGCACATCATGGT

PIK3CA H1047R mut-probe: TGATGCACGTCATGGT

Western blots

Protein concentration was determined using the Pierce BCA Protein Assay Kit (Thermo Scientific Cat#23225). For immunoblots, equal protein amounts were loaded and then separated by electrophoresis through NuPAGE Novex Bis-Tris 4-12% gradient gels (Invitrogen) and

MOPS SDS buffer, with the SeeBlue™ Plus2 Pre-stained Protein Standard (ThermoFisher Cat# LC5925) serving as the molecular weight marker. However, the detection of ubiquitinated p110α is an exception. To achieve proper separation of this modified protein, we used a 3-8% Tris Acetate gel run in Tris Acetate SDS buffer. In these specific instances, the HiMark™ Pre-stained Protein Standard (ThermoFisher Cat# LC5699) was used as the molecular weight marker. Proteins were transferred onto Nitrocellulose membranes using the iBlot system and protocol from InVitrogen (Carlsbad, CA). Membranes were blocked for 1 h in 5% milk in TBST (20mM Tris-HCL pH7.5, 135 mM NaCl, 0.1% Tween20) at room temperature (RT) and incubated overnight with the primary antibody at a 1:1000 dilution in 5% milk TBST at 4°C with agitation. The membranes were washed three times, 5 min each with TBST. After 1 h of incubation at RT with the 1:10000 diluted anti-mouse (Jackson ImmunoResearch) or anti-rabbit (Jackson Immuno Research) HRP-conjugated secondary antibodies, the membranes were washed three times in TBST and bands were detected using ECL (Bio-Rad) and autoradiography film (Amersham Biosciences, GE Healthcare) exposure.

Ubiquitin pull-down assay

Cells were lysed in 20 mM TrisHCL pH 7.5, 137 mM NaCl, 1 mM EDTA, 1% NP40, 10% glycerol plus protease and phosphatase inhibitors. For the ubiquitinated protein pulldown experiment, cells were lysed in a lysis buffer containing 200 µg/mL TUBE1 (Lifesensors UM101). Lysates were isolated and 50 µL of glutathione agarose beads were added to them (Sigma, G4705). The samples were incubated overnight and captured ubiquitinated protein was eluted in SDS reducing sample buffer.

Subcellular fractionation

Cells were washed once with phosphate-buffered saline, before scraping into 0.8 ml/dish hypotonic lysis buffer (HLB: 25 mM Tris–HCl pH7.5, 10 mM Nacl, 1 mM EDTA, protease and phosphatase inhibitors). The cells were lysed by 30 strokes in a Dounce homogenizer, subjected to centrifugation at 1500 g (3000 RPM) for 5 min to pellet nuclei and unbroken cells, followed by centrifugation of the supernatant at 100,000 g (44,000 RPM) in TLA55 rotor for 40 min. The supernatant (800 µL) was collected (S100 fraction) and the pellet resuspended in 200 µL HLB plus 1% NP40 (P100 fraction). The resuspended pellet was centrifuged 5 min in high speed in microfuge and supernatant collected.

Immunoprecipitation and pull down

Cells were lysed in 20 mM TrisHCL pH 7.5, 137 mM NaCl, 1 mM EDTA, 1% NP40, 10% glycerol plus protease and phosphatase inhibitors. For the immunoprecipitation of p85β, 1 mg of prepared lysates were incubated with antibodies (Abcam, Cat# ab28346, RRID:AB_777251) at a dilution of 1:100 at final volume of 1ml overnight. Next, 50 µL of protein A agarose beads were added to each sample and incubated an additional 2 h. For HER3 and FGFR2 immunoprecipitation, lysates were incubated overnight with a biotin-conjugated HER3 or FGFR2 antibody, respectively (Invitrogen, Cat# MA5-13037, RRID:AB_10983790; and OriGene, Cat# TA502917AM), which was followed by the addition of 50 µL of streptavidin agarose beads to each sample and an additional 2 h incubation. For RAS immunoprecipitation, cells were lysed in IP lysis buffer (25 mM Tris HCL pH 7.5, 150 mM NaCl, 1 mM EDTA, 1% NP40, 5 mM $MgCl_2$, 10% glycerol, protease and phosphatase inhibitors) and collected on

ice. Lysates were spun at 14000 rpm for 10 mins at 4^{o}C and supernatant was collected. Lysates were quantified using the Pierce™ BCA Protein Assay Kits (Thermo Scientific Cat# 23225). Soluble proteins (1 mg) were subjected to immunoprecipitation with either 12 µL (6 µL of packed beads) of washed anti-RAS magnetic beads (Millipore Cat# 16-321) or mouse anti-IgG magnetic bead conjugate (Cell Signaling Technology Cat# 5873S) as a control and incubated at 4^{o}C for 5 h. The complex was washed 3x with 1 mL of cold IP lysis buffer. Washed beads were resuspended in 50 µL of sample buffer.

FGFR2 stable cell line generation

T47D breast cancer cells were engineered using CRISPR to knock out *PIK3CA* WT allele to create T47D *PIK3CA* mutant cell line using the method previously described (14). FGFR2 WT and FGFR2 N550K cDNA were synthesized and cloned into doxycycline- (dox) inducible PiggyBac transposase expression vector with constitutive mCherry expression. Cells (~2 x10^{5}) were transfected with 750 ng of transposon vector (FGFR2 WT or FGFR2 N550K) and 250 ng of piggyBac transposase in 6-well culture plates. After 48 hours, cells were detached and replated in T175 flasks. Once confluent, mCherry expression was selected by flow cytometry and clones were expanded to create stable lines. Expression of FGFR2 was validated by qRT-PCR using FGFR2 primers and probes (Applied biosystems).

RTK array

Total protein was extracted using the lysis buffer provided by Human Phospho RTK-array kit (R&D Systems). Protein concentrations were determined and 300 µg of total protein

was incubated overnight at 4ºC with array membranes. After washing, array membranes were incubated with Anti-Phospho-Tyrosine-HRP Detection Antibody (provided in the kit) for 2 h at RT with agitation. pRTK was detected with Chemi Reagent Mix and autoradiography film.

Live cell imaging by IncuCyte®

Cells were cultured and plated into 96-well plates at a density of 2000 cells per well. The next day, inhibitors were added at indicated concentrations. Every 7 days, the media was aspirated and replaced with fresh media with or without inhibitors. Cells were imaged every 4 h in IncuCyte® Zoom (Essen Bioscience). Phase-contrast images were collected and analyzed for cell proliferation. The cell confluence of 6 replicate wells was determined for the duration of the experiment.

***In vivo* xenograft studies**

Female NCR nude mice were obtained from Taconic Biosciences and housed at Genentech according to standards established by the Institutional Animal Care and Use Committee. Human MFM223x2.2 mammary carcinoma cells were cultured *in vitro,* harvested in log-phase growth, and resuspended in Hank's Balanced Salt Solution (HBSS) containing Matrigel (BD Biosciences; San Jose, CA) at a 1:1 ratio by volume for *in vivo* inoculation. Mice were implanted with 17ß-Estradiol pellets (0.36 mg, 60 d release, Innovative Research of America, SE121) subcutaneously in the left flank, 1-3 days prior to inoculation. Mice were then inoculated in the right mammary fat pad 2 with 10×10^6 MFM223x2.2 cells in a total volume of 100 µL. Tumors are allowed to grow to a volume in an initial range before mice are randomized

to treatment groups at the start of dosing to create closely matched baseline average tumor sizes across regimens.

For pharmacodynamics study, mice (*n*=4-5 per group) were given by oral gavage FGFR2i (1 mg/kg, 10 mg/kg or 20 mg/kg) daily for 4 days; tumors were collected 6 hours post last dose. For efficacy study, mice (*n*=8 per group) were given by oral gavage FGFR2i (10 mg/kg or 20 mg/kg) and/or inavolisib (25 mg/kg) daily for 22 days. FGFR2i is formulated in 60% Polyethylene glycol 400 (PEG400), 1 eq. Hydrochloric Acid (HCl) and/or inavolisib are formulated in 0.5% Methylcellulose and 0.2% Tween 80.

Tumor sizes and mouse body weights were recorded twice weekly over the course of the study. Tumor volumes were measured in two perpendicular dimensions (length and width) using Ultra Cal-IV calipers (model 54 − 10 − 111; Fred V. Fowler Co.; Newton, MA) and calculated according to the following formula: Tumor size (mm^3) = (longer measurement × shorter measurement^2) × 0.5. Animal body weights were measured using an Adventura Pro AV812 scale (Ohaus Corporation; Pine Brook, NJ). Percent animal weight change was calculated using the following formula: Body weight change (%) = [(current body weight/initial body weight)−1) × 100]. Analyses and comparisons of tumor growth were performed using a package of customized functions in R (Version 3.6.2); R Foundation for Statistical Computing; Vienna, Austria., which integrates software from open-source packages as described in Forrest et al (26). Growth contrast represents the difference in area under the curve (AUC)-based growth rates (endpoint Gain Integrated in Time (eGalT)) between the treatment and reference group (26). Contrast values <1 indicate an antitumor effect; the smaller the value below 1, the greater the

magnitude of the antitumor effect. The 95% CIs are based on the fitted model and variability measures of the data.

Data sharing

To request access to clinical data that support the findings of this study, see here (https://vivli.org/members/enquiries-about-studies-not-listed-on-the-vivli-platform/), and for up-to-date details on Roche's Global Policy on the Sharing of Clinical Information, see here (https://www.roche.com/innovation/process/clinical-trials/data-sharing/). The data supporting the findings of this study that have been originated by Foundation Medicine, Inc. are de-identified data that may be made available upon request and are subject to a license agreement with Flatiron Health and Foundation Medicine; interested researchers should contact cgdb-fmi@flatiron.com to determine licensing terms.

RESULTS

Clinical profile of inavolisib monotherapy

Between December 2016 and January 2019, 19 female patients with HR+/HER2− breast cancer and one male patient with colorectal cancer were enrolled in a 3+3 design dose-escalation study using 6 mg (*n*=7), 9 mg (*n*=9), and 12 mg (*n*=4) QD oral inavolisib dose cohorts (Fig. 1A; Supplementary Table S3). Key eligibility criteria included the presence of at least one *PIK3CA*mut in tumor tissue or ctDNA, fasting glucose ≤140 mg/dL, and HbA1c <7%. The median age was 65 years (range 41–77), and 11 patients (55%) had Eastern Cooperative Oncology Group (ECOG) Performance Status score of 0 at baseline. Five patients (25%) were obese (BMI ≥30 kg/m^2) overall, including two patients (50%) in the 12 mg cohort. Racial and ethnic diversity was limited in this small-sized study (Table 1). The median number of prior cancer therapies in the metastatic setting was 3 (range 1-10). Most patients were previously treated with chemotherapy (*n*=19, 95%) as well as a cyclin-dependent kinase 4 and 6 (CDK4/6) inhibitor (*n*=18, 90%), aromatase inhibitor (*n*=19, 95%), and/or the selective estrogen receptor degrader (SERD) fulvestrant (*n*=13, 65%). Notably, none of the patients were previously treated with PI3K inhibitors. The median inavolisib treatment duration was 3.8 months (range 1.1−17.6) and median cumulative dose intensity was 97% (range 46%−101%). Five (25%) patients received treatment beyond 200 days.

The maximum tolerated dose (MTD) of inavolisib was 9 mg QD; two out of four dose-limiting toxicity (DLT)-evaluable patients in the 12 mg dose group experienced DLTs, including Grade 4 hyperglycemia and Grade 3 fatigue that lasted 5 days; AEs were graded according to the National Cancer Institute Common Terminology Criteria for Adverse Events (NCI-CTCAE) v4.

All patients discontinued study treatment due to disease progression (Response Evaluation Criteria in Solid Tumors [RECIST] v1.1, *n*=16, 80%) and clinical progression (*n*=4, 20%). One death on study was due to disease progression during the safety follow-up.

Overall, 19 (95%) patients had at least one AE related to inavolisib (Table 2), the most common (≥15%) of which were hyperglycemia (70%), diarrhea (45%), decreased appetite, stomatitis (grouped term: stomatitis, mucosal inflammation, and palatal ulcer), vomiting (20% each), fatigue, nausea, weight decrease, and alopecia (15% each). Eight (40%) patients had at least one Grade 3−5 AE related to inavolisib, including hyperglycemia (20%), fatigue, nausea, weight decrease, asthenia, and lymphopenia (5% each). One patient experienced a serious AE related to inavolisib (Grade 4 hyperglycemia) in the 12 mg cohort, which was downgraded to Grade 3 the same day and resolved within 6 days following treatment with oral antihyperglycemic medication. Treatment-related rash occurred in one (5%) patient (Grade 1). Treatment-related stomatitis (grouped term) occurred in four (20%) patients (all Grade 1) and generally responded to oral corticosteroid mouthwash. Eleven (55%) patients had at least one AE related to inavolisib leading to dose modification in the 6 mg (*n*=4), 9 mg (*n*=3), and 12 mg (*n*=4) dose cohorts, with 13 events that included 7 interruptions and 6 reductions (no discontinuations). No treatment-related grade ≥3 gastrointestinal toxicities were reported, and treatment-related diarrhea events were Grade 1-2. Colitis was not observed with inavolisib monotherapy, including in the nine patients on treatment for ≥5 months. No Grade 5 AEs were reported.

Twenty patients were included in the PK analysis and the data were summarized according to treatment dose level. Patients received their first dose on C1D1, followed by a 7-

day washout period and frequent PK sampling. QD dosing was resumed on C1D8. Plasma exposure of inavolisib increased in a dose-proportional manner following single and multiple doses (Fig. 1B). Mean half-life ($t_{1/2}$) following a single dose was 16 hours. With continuous once-daily dosing, there was a ~2-fold accumulation, consistent with the observed $t_{1/2}$ and the dosing frequency. At the MTD (9 mg), inavolisib inter-subject PK variability was low for C_{max} and $AUC_{0\text{-}24}$ after a single dose as well as at steady state (%CV ~20-40%).

Matched pre-treatment (baseline) and on-treatment (C1D15) biopsy samples from nine patients were evaluable for pharmacodynamic (PD) response to study treatment by immunohistochemistry (IHC). With some exceptions, this analysis illustrated a consistent decrease in PI3K pathway activity based on reduced H-scores for phosphorylated AKT (pAKT) and phosphorylated ribosomal protein S6 (pS6) as well as reduced proliferation as assessed by Ki67 nuclear staining (Fig. 1C).

Given that PI3K inhibition modulates cellular glucose uptake, PD response was also evaluated by ^{18}F-fluorodeoxyglucose positron emission tomography (FDG-PET). All 20 patients had FDG-avid disease on pre-treatment (baseline) scans, and 16 (75%) achieved a partial metabolic response (PMR) on scans acquired after 2 weeks of inavolisib QD (Fig 1D). Metabolic responses were seen at all dose levels with a trend toward more frequent and deeper responses at higher doses, that is a PMR in 4/7 (57%) and mean of 25% reduction in uptake at 6 mg versus a PMR in 12/13 (92%) and mean of 43% reduction in uptake with >6 mg (Fig. 1D).

Reflective of the eligible *PIK3CA* hotspot mutations for this trial (see Methods), *PIK3CA*mut primarily occurred in the helical (*n*=8, 40%) and kinase (*n*=6, 30%) domains of p110α; one patient (5%) had a missense mutation resulting in a N345K substitution in the C2

domain and five (25%) patients' tumors exhibited more than one *PIK3CA*mut. From analysis of ctDNA, decreased *PIK3CA* mutant allele frequency (MAF) was observed over time between pre- and on-treatment timepoints in the majority of paired specimens, particularly in those from patients who experienced a partial response (Fig. 1E).

Twenty patients were evaluated for response, including 19 patients with measurable disease at baseline, and were assessed for radiographic response utilizing RECIST v1.1. Among patients with measurable disease (*n*=19), the best overall response was partial response (PR) in five (26%) patients, and the confirmed objective response rate was 21% (Fig. 1F). The duration of response was 3.7 months (95% confidence interval [CI]: 3.0, NE) among the responders with a confirmed response. The clinical benefit rate (defined as percentage of patients with confirmed complete response (cCR), PR, and those with ≥24 weeks duration of stable disease (SD) or non-complete response/non-progressive disease (non-CR/non-PD) since first study treatment for single-agent inavolisib (*N*=20) was 45% (*n*=9). The median progression-free survival (PFS) was 3.7 months (95% CI: 3.5, 7.3). The landmark progression-free rate at 6 months was 37% (95% CI: 15, 59).

***FGFR2* mutations are associated with clinical benefit**

To better understand the genomic alterations associated with response to inavolisib, we performed targeted sequencing of ctDNA from available longitudinal plasma samples from the 20 patients. We found *FGFR2* short variant (SV) mutations in pre-treatment liquid biopsy samples from two of the nine patients who experienced clinical benefit during the study as defined above (Fig. 2A, Supplementary Fig. S1; see methods). These missense mutations

translated into a P253R substitution in the FGFR2 extracellular domain and a N549K substitution in the FGFR2 kinase domain, both of which are known to result in constitutive activation of the receptor (18,27) (Fig. 2A, Supplementary Table S4). *FGFR2* alterations were not observed in patients who did not receive clinical benefit from single-agent inavolisib (Supplementary Fig. S1). *PTEN* loss-of-function mutations were present in samples from two of the nine patients who received clinical benefit as well as in samples from two of the 11 patients who did not receive clinical benefit from single-agent inavolisib. Additionally, we found activating AKT1 E17K mutations in three patients who did not receive clinical benefit (Fig. 2A, Supplementary Fig. S1, Supplementary Table S4).

To validate the possible cooperation between *PIK3CA* and *FGFR2* alterations within a large oncogenomic dataset, we first identified FGFR2 N549 (D/H/K/T) hotspot mutations in tumor biopsies from nearly 50,000 patients with breast cancer that underwent comprehensive genomic profiling (CGP) during the course of routine clinical care (28) (Fig. 2B). FGFR2 N549 short variant (SV) alterations occurred in 0.37% of breast cancer samples. We then examined driver alterations including *PIK3CA* hotspot mutations and their incidence in *FGFR2*-mutant breast cancers. Interestingly, *PIK3CA* mutations showed the strongest co-occurrence with *FGFR2* SVs (Fisher's exact test, odds ratio (OR)=4.0, adjusted $p<0.0001$; Fig. 2C; Supplementary Fig. S2A), in accordance with previous reports (18). This co-occurrence was further strengthened when *FGFR2* mutations affecting the tyrosine kinase domains were sub-selected (Fisher's exact test, OR=6.7, adjusted $p<0.0001$; Supplementary Fig. S2B). Consistent with other literature, *PIK3CA*mut primarily occurred in the helical and kinase domains

(Supplementary Fig. S2C-D) (29-31); both single and multiple *PIK3CA*mut SVs co-occurred with *FGFR2* alterations (Supplementary Fig. S2C).

Cells harboring multiple *PIK3CA*mut are associated with increased sensitivity to p110α inhibition as compared to cells harboring only a single *PIK3CA*mut (10). Therefore, using the CGP dataset (28), we evaluated the association of different *PIK3CA*mut categories (i.e. single, multiple *PIK3CA*mut) with *FGFR2* SVs and other types of alterations, that is, rearrangements (REs), copy number alterations (CNAs), and variants of unknown significance (VUS). (Supplementary Fig. S3A). In tumors categorized as HER2−, we observed a statistically significant relationship between *FGFR2* alterations and various *PIK3CA*mut categories (Supplementary Fig. S3B); in particular, we observed a significant co-occurrence between single *PIK3CA*mut and known or likely oncogenic *FGFR2* SVs (OR=3.6, FDR<0.05) as well as known or likely oncogenic structural *FGFR2* alterations (CNAs or REs; OR=1.5, FDR<0.05). Multiple *PIK3CA*mut SVs were significantly concurrent with *FGFR2* SVs (OR=2.0, FDR<0.05), but were mutually exclusive of *FGFR2* CNAs (OR=0.4, FDR<0.05). The same analysis across samples representative of all solid tumor types demonstrated that both single *PIK3CA*mut and multiple *PIK3CA*mut significantly co-occur with *FGFR2* alterations of any type (SVs, OR=1.8, FDR<0.05; CNAs and/or REs, OR=3.1, FDR<0.05; Supplementary Fig. S3C).

FGFR2 alterations and sensitivity to inavolisib

Based on the findings in the clinical trial samples and the CGP dataset (Figs. 1 and 2A-C), we functionally examined whether *FGFR2* mutation status and *PIK3CA* driver mutations were associated with increased sensitivity to inavolisib. To this end, we correlated oncogenomic

and RNA sequencing-derived transcriptomic profiles and inavolisib drug-response data across 736 PRISM cell lines from all tumor indications with different presentations of the two genes (hotspot alterations, other alterations, and wildtype [WT]) (22). Cell lines containing *PIK3CA* hotspot mutations were significantly more sensitive to inavolisib as compared to cell lines that contained non-hotspot *PIK3CA* mutations or were WT for *PIK3CA* (WT + other; Fig. 2D). However, the presence of *FGFR2* hotspot alterations, that is, SVs, focal amplifications, and/or exon 18 (E18)-truncating rearrangements (18), in *PIK3CA*mut cell lines did not further increase sensitivity to inavolisib versus cell lines without *FGFR2* hotspot aberrations (Fig. 2D). Apart from *FGFR2* mutations, high expression drives FGFR2 oncogenicity and is predictive of response to FGFR-targeted therapies (18,19,32). *FGFR2* gene expression in *FGFR2* hotspot mutant cell lines versus other cell lines was increased (Supplementary Fig. S4A), as previously observed (18). Across the PRISM cell line panel, *FGFR2* expression also correlated with PI3K-AKT signaling pathway activation, as revealed by phospho-AKT reverse phase protein array (RPPA) profiling (R=0.23, $p<0.0001$, Supplementary Fig. S4B). Upon analyzing FGFR2 expression and inavolisib drug-response values, we observed a moderate association between FGFR2 expression and inavolisib sensitivity (R=−0.21, $p<0.0001$, Fig. 2E). Cell lines expressing higher levels of FGFR2 based on transcript levels are significantly more sensitive to inavolisib as compared to lower expressing cell lines (Supplementary Fig S4C). Notably, *PIK3CA*mut cell lines with co-occurring high FGFR2 expression were most sensitive to inavolisib (Fig. 2E). The comparison of inavolisib dose-response values in *PIK3CA*mut versus remaining cell lines and in top versus bottom tertile of FGFR2-expressing lines revealed that the concomitant presence of a *PIK3CA* hotspot mutation and high FGFR2 expression conferred particular sensitivity to

inavolisib (Fig. 2F). Taken together, these data show that *PIK3CA* hotspot mutant tumor cells with high FGFR2 expression levels – potentially promoted by *FGFR2*-activating alterations – are especially sensitive to inavolisib.

High FGFR2 expression confers dependence on the PI3K pathway

To better understand how *FGFR2* mutation status and expression influence sensitivity to inavolisib, we first selected 16 cell lines that capture the genomic heterogeneity of *FGFR2* observed in cancer, including *FGFR2* hotspot missense mutations, focal amplifications, and REs resulting in E18-truncations (18). Western blotting showed a differential abundance and substantial overexpression of FGFR2 protein in six of the 16 cell lines. The six FGFR2 top-expressing cell lines were designated FGFR2-high, whereas the remaining 10 lines were designated FGFR2-low (Fig. 2G). High FGFR2 expression was present amidst concurrent expression of other FGFR paralogs (Fig. 2G). To identify differential dependencies on the four FGFR paralogs across the *FGFR2*-altered cell lines, we depleted *FGFR1*, *2*, *3*, or *4* transcripts using silencing RNAs (siRNAs; Supplementary Fig. S4D). *FGFR2* expression levels correlated with sensitivity to FGFR2 silencing, with the FGFR2-high cell lines being the most FGFR2 knockdown-sensitive (Fig. 2H). In contrast, the cell lines were less dependent on the other FGFR paralogs and sensitivity to siRNA-targeting of the FGFRs did not correlate to the expression levels of the respective *FGFR* transcripts (Fig. 2H). Consequently, FGFR2-high cell lines were significantly more sensitive to *FGFR2* siRNA treatment as compared to the FGFR2-low lines (Fig 2I), suggesting that, apart from *FGFR2* alteration status, the FGFR2 expression level determines the magnitude of dependency on this RTK.

We made use of a highly selective FGFR2 small-molecule inhibitor (FGFR2i) (33). This tool compound specifically blocks FGFR2 kinase activity, but not the activity of FGFR1, 3, or 4, as demonstrated by enzymatic assays (Fig. 2J upper panel). We compared the activity of the tool FGFR2i to infigratinib, a highly potent but non-selective pan-FGFR inhibitor (34). In dose-response proliferation assays, the tool FGFR2i was significantly more potent in FGFR2-high versus FGFR2-low cell lines as measured by GR50 values (p=0.0074, Wilcoxon's rank sum test; Fig. 2J and Supplementary Fig. S5A). In particular, SUM52PE cells, which harbor focal *FGFR2* amplification that results in high expression of E18-truncated, oncogenic FGFR2 (18) were highly sensitive to the FGFR2i (Supplementary Fig. S5A). In contrast, all three FGFR2-high cell lines (SUM52PE, MFE296, and AN3CA) as well as the FGFR2-low cell line MFE280 were sensitive to infigratinib (Supplementary Fig. S5A). Next, we assessed the effects of both inhibitors on FGFR signaling. In SUM52PE, MFE296, and AN3CA cells, the FGFR2i and infigratinib showed equal potency in reducing phosphorylation of FGFR and its downstream signaling effectors FRS2α, PLCγ, AKT, and ERK. Conversely, in MFE280 cells, these targets were inhibited to a lesser extent by the tool FGFR2i as compared to infigratinib (Supplementary Fig. S5B). These results supported the observation that FGFR2-high cell lines primarily depend on FGFR2 and to a negligible extent on other FGFRs and suggested that FGFR2-low lines are either FGFR-independent or depend on FGFR paralogs other than FGFR2.

Next, we ranked *PIK3CA*mut cell lines according to *FGFR2* mRNA expression using the "Dependency Map" data (35), and we selected 29 cell lines that represent the spectrum of *FGFR2* expression found across different cancer types (Supplementary Fig. S6A). We verified protein expression levels of the four FGFR paralogs as well as HER2 and HER3 that are known

upstream regulators of the PI3K pathway (14). *FGFR2* mRNA was detected in all 29 cell lines (Supplementary Fig. S6A), yet FGFR2 protein was detectable via Western blotting only in the top 12 *FGFR2* mRNA-expressing cell lines (Supplementary Fig. S6B). We subjected the 29 cell lines to inavolisib dose-response assays (Supplementary Fig. S6C). Grouping the cell lines into FGFR2-high and FGFR2-low categories based on FGFR2 protein expression levels (Supplementary Fig. S6B) showed that the majority of the FGFR2-high cell lines were sensitive to inavolisib. A few FGFR2-low cell lines were insensitive to inavolisib, however a larger fraction of FGFR2-low cell lines showed high sensitivity to inavolisib that was comparable to that observed in FGFR2-high lines (Supplementary Fig. S6C). We analyzed the oncogenomic profiles of the 29 *PIK3CA*mut cell lines and identified secondary mutations in *PIK3CA*, focal amplifications of *PIK3CA*, *ERBB2* (encodes HER2), or *KRAS*, as well as *RASA1* loss-of-function (lof) alterations (Fig. 3A). *ERBB2* amplifications observed in seven FGFR2-low cell lines correlated with high p-HER2 levels in five out of six cell lines as identified by Western blotting (Fig. 3A and Supplementary Fig. S6B). These oncogenic alterations represented drivers that may cooperate with mutated p110α to potentiate PI3K signaling and sensitivity to PI3K targeting (8-10,14,34,36) and appeared to be mutually exclusive of high levels of FGFR2 (Fig. 3A). Indeed, FGFR2-high cell lines were similarly sensitive to inavolisib as compared to the FGFR2-low cell lines that express high pHER2. However, the presence of secondary *PIK3CA* or RAS-activating alterations did not correlate with increased inavolisib sensitivity. Notably, the remaining FGFR2-low cell lines devoid of PI3K signaling-augmenting alterations displayed weak responses to inavolisib. (p=0.044; Wilcoxon's rank sum test; Fig. 3A-B).

FGFR2 activation of PI3K signaling

Based on the oncogenomic correlates identified in *PIK3CA*mut cell lines, we set out to mechanistically decipher the FGFR2-PI3K signaling network. HER3 is a receptor that is known to activate the PI3K regulatory subunit p85β by direct binding (37). HER3 lacks intrinsic tyrosine kinase activity, and therefore, typically forms heterodimers with other RTKs, such as HER2, to mediate signaling transduction through the PI3K-AKT pathway (38-40). We explored whether FGFR2 might interact with HER3 to stimulate PI3K signaling in a *PIK3CA*-mutated context. We focused on the two FGFR2-high cell lines SUM52PE and MFM223, both of which express E18-truncated, oncogenic FGFR2 (18), and the FGFR2-low but HER2-dependent cell line MFE280, all of which are highly sensitive to inavolisib (Fig. 3B and Supplementary Fig. S6D). The three cell lines had a similar pattern of basal RTK phosphorylation as evaluated by phospho-RTK profiling (Supplementary Fig. S6E). Upon treatment with the FGFR2i tool compound, in SUM52PE and MFM223 FGFR2-high cell lines, we observed a substantial reduction of the phosphorylation of FGFR2, as well as of HER3. In contrast, the FGFR2i had no effect on HER3 phosphorylation in MFE280 FGFR2-low cells (Fig 4A-B and Supplementary Fig. S6E). Conversely, treatment with the HER2 inhibitor lapatinib resulted in decreased phosphorylation of HER3 and AKT solely in the FGFR2-low, HER2-dependent MFE280 cells (Fig. 4B). While 1 h inavolisib treatment showed no feedback induced pHER3 expression, 24 h treatment moderately induced pHER3 Y1289 and Y1328 expression in FGFR2 high cell lines (SUM52PE and MFM223). FGFR2i treatment blocked feedback induced pHER3 Y1289 in the SUM52PE but less in the MFM223 cell line. In contrast, treatment with FGFR2i blocked pHER3 Y1328 in FGFR2 high cell lines at all time points studied (Supplementary Fig. S7A).

These results confirmed that in FGFR2-high cancer cells, FGFR2 activates PI3K signaling through HER3 to sustain PI3K activity.

We next tested whether the inhibition of FGFR2 prevents HER3-PI3K interaction and pathway activation. We performed co-immunoprecipitation of the PI3K regulatory subunit p85β in SUM52PE, MFM223, and MFE280 cells and detected a strong interaction between p85β and HER3 (Fig. 4C). Treatment with inavolisib did not affect binding of p85β to HER3, whereas the tool FGFR2i blocked this interaction specifically in FGFR2-high SUM52PE and MFM223 cells, resulting in reduced phosphorylation of AKT (Fig. 4C). Co-immunoprecipitation of HER3 confirmed loss of the HER3-p85β interaction upon treatment with the FGFR2i (Supplementary Fig. S7B). Notably, the FGFR2i did not affect the HER3-p85β interaction in MFE280 FGFR2-low cells (Fig. 4C and Supplementary Fig. S7B). However, in these cells, lapatinib suppressed binding of p85β to HER3 (Supplementary Fig. S7B), consistent with the high HER2 levels and the HER2-dependent HER3-PI3K activation (14).

To further evaluate whether FGFR2 depends on HER3 to signal through PI3K, we silenced HER3 using RNAi. Interestingly, loss of HER3 only partially reduced AKT phosphorylation in SUM52PE and MFM223 cells (Supplementary Fig. S7C), suggesting that FGFR2 does not wholly rely on HER3 to activate PI3K signaling. RTKs such as FGFR2 can also induce the PI3K signaling cascade through RAS (41). Pulldown of GTP-bound RAS showed that the FGFR2i causes a decline in RAS-GTP levels in the MFM223 FGFR2-high cells, whereas RAS-GTP levels remained unchanged in the MFE280 FGFR2-low cells (Fig. 4D). RAS co-immunoprecipitation further showed that inhibition of FGFR2 effectively impaired the interaction of RAS with the p110α PI3K catalytic subunit in MFM223 cells (Fig. 4E). However,

in MFE280 cells, FGFR2 blockade did not interfere with the RAS-p110α interaction (Fig. 4E). Notably, lapatinib treatment affected neither RAS-GTP levels nor the RAS-p110α interaction in the MFM223 or MFE280 cells (Fig. 4D-E). This suggests that HER2 primarily relied on HER3 to activate PI3K, whereas FGFR2 depends on both HER3 and RAS to mediate PI3K signaling (Fig. 4F).

Next, we examined whether FGFR2 directly interacts with HER3. SUM52PE and MFM223 FGFR2-high cells were treated with inavolisib, the FGFR2i, or lapatinib, and subjected to co-immunoprecipitations. HER3 confirmed to interact with p85β, as expected (Fig. 4G). FGFR2 also interacted with p85β, but did not interact with HER3 or p85α (Fig. 4G and Supplementary Fig. S7D). Blockade of FGFR2 activity using the FGFR2i perturbed the interaction between p85β and FGFR2 (Fig. 4G), whereas neither inavolisib nor lapatinib treatment interfered with the FGFR2-p85β or the HER3-p85β interactions (Fig. 4G and Supplementary Fig. S7B). These findings propose that PI3K regulatory subunit acts as a direct effector protein of FGFR2, and suggested that FGFR2 engages RAS as well as HER3 to mediate PI3K signaling.

Effects of FGFR2 signaling on sensitivity to inavolisib

In HER2+ *PIK3CA*-mutated cancer, inavolisib appears to promote the degradation of mutated p110α in an RTK-dependent manner; that is, HER2-HER3 recruits mutated PI3K to the cell membrane to promote p110α ubiquitination and degradation, resulting in sustained PI3K pathway inhibition (14). We hypothesized that similar to HER2, FGFR2 activity engaging HER3 may lead to inavolisib-induced ubiquitination of mutated p110α. Indeed, treatment with

inavolisib induced ubiquitination of p110α in the *PIK3CA*mut cell lines MFM223 and MFE280, whereas p110α showed no ubiquitination in the *PIK3CA* WT cell line SUM52PE (Fig. 4H). The FGFR2i blocked p110α ubiquitination specifically in *PIK3CA*mut and FGFR2-high MFM223 cells. Notably, in FGFR2-low but HER2+ MFE280 cells, lapatinib prevented p110α ubiquitination (Fig. 4H). To validate these findings and to measure mutated p110α degradation independently of a WT allele, we engineered the HR+/HER2− and p110α H1047R heterozygously mutated T47D breast cancer cell line to express only the H1047R allele via CRISPR/Cas9 deletion of the WT allele. Specific loss of the *PIK3CA* WT allele was confirmed at the RNA level (Supplementary Fig. S7E). We then introduced dox-inducible *FGFR2* WT or *FGFR2* N550K hotspot mutant constructs into the *PIK3CA* H1047R isogenic line. Overexpression of both WT and N550K FGFR2 led to comparable pathway activation, as demonstrated by phosphorylation of FRS2, HER3, PLCγ, and AKT (Supplementary Fig. S8A left panel). Inavolisib treatment promoted mutated p110α ubiquitination in cells overexpressing either FGFR2 variant, whereas control vector-expressing cells showed no p110α ubiquitination (Supplementary Fig. S8A right panel). Downstream pathway signaling and HER3 phosphorylation were reduced and increased, respectively, in FGFR2 WT- and N550K-expressing cells upon inavolisib treatment, although FGFR2 N550K-expressing cells appeared to be more affected by inavolisib than the control or FGFR2 WT-expressing cells (Supplementary Fig. S8A left panel). FGFR2i treatment blocked inavolisib-mediated ubiquitination of H1047R-mutated p110α in FGFR2 N550K-expressing cells (Supplementary Fig. S8B). Extended inavolisib treatment resulted in the degradation of mutated p110α protein in FGFR2 N550K-overexpressing cells, but not in the matched control cells (Supplementary Fig. S8C). The

proteasome inhibitor MG132 rescued inavolisib-induced mutated p110α degradation (Supplementary Fig. S8D). Notably, ectopic expression of FGFR2 N550K resulted in moderately increased sensitivity to either the FGFR2i or inavolisib as compared to the respective controls (no DOX vs. plus DOX) (Supplementary Fig. S8E).

In *PIK3CA*mut MFM223 cells, treatment with the non-degradation inducing p110α inhibitor alpelisib, pAKT rebounded after 30 min and continued to accumulate for 24 h. In contrast, pAKT reactivation was markedly delayed with inavolisib treatment and observed only 24 h post treatment start (Fig. 4I). In *PIK3CA* WT SUM52PE cells, a similar PI3K pathway feedback response was observed after treatment with either alpelisib or inavolisib (Fig. 4I). Consistently, the difference in potency between the mutated p110α-degrading inavolisib and the non-degrading inhibitor alpelisib was significantly larger in *PIK3CA*mut cell lines expressing high levels of FGFR2 compared to FGFR2-low cell lines, as measured by the ratio of GR50 values ($p=0.035$, Wilcoxon's rank sum test); (Fig. 4J). The strength of inhibitor-induced pathway feedback appears dependent on the amount of RTK expression. As predicted, T47D-engineered cells overexpressing FGFR2 but not the matched control cells, displayed pAKT rebound only during alpelisib treatment, whereas treatment with inavolisib led to sustained pathway inhibition (Supplementary Fig. S8F). Collectively, these data provided evidence that high expression of FGFR2, and especially mutated FGFR2, dictates the cellular response to inavolisib by facilitating mutated p110α degradation.

Combined inhibition with inavolisib and FGFR2i

We next assessed whether the sensitivity to inavolisib in FGFR2-high cell lines could be potentiated by co-targeting FGFR2. Silencing of *FGFR2* with RNAi increased sensitivity to inavolisib in five of the six lines tested (Fig. 5A and Supplementary Fig. S9A). In contrast, the depletion of other *FGFR* paralogs in FGFR2-high cell lines as well as the silencing of FGFR2 or other FGFRs in FGFR2-low cell lines had no effect on sensitivity to inavolisib (Fig. 5A and Supplementary Fig. S9B). We co-treated FGFR2-high and -low cell lines with inavolisib and the tool FGFR2i. Consistent with the *FGFR2* knockdown results, we found that FGFR2i synergizes with inavolisib particularly in FGFR2-high cell lines, as determined by Bliss scores and a fixed dose ratio method (Fig 5B, Supplementary Fig. S10A-B, Supplementary Table S5). The non-selective pan-FGFR inhibitors infigratinib, AZD4547 (42), and LY2874455 (43) synergized with inavolisib in a similar manner (Supplementary Fig. S11).

Finally, we evaluated how silencing different *FGFR* paralogs affected the PI3K signaling network activity during inavolisib treatment. In the FGFR2-high cell lines SUM52PE and ANC3A, *FGFR2* depletion using siRNA led to a particularly profound suppression of the phosphorylation of the PI3K downstream effectors AKT, 4E-BP1, and ERK, as compared to inavolisib alone (Fig 5C). These results suggested that patients with cancers that harbor *PIK3CA* mutations and FGFR2 overexpression may benefit from combined therapy with inavolisib and an FGFR2 inhibitor.

Combination treatment regression and resistance delay

Prompted by the *in vitro* data, we next assessed the activity of the tool FGFR2i in combination with inavolisib using the MFM223 X2.2 tumor xenograft model. This *in vivo* model is derived from the MFM223 cell line that contains the p110α H1047R hotspot mutation and focal *FGFR2* amplification resulting in the expression of E18-truncated FGFR2 (18). We treated immunocompromised mice bearing xenografted MFM223 X2.2 with either vehicle control or the tool FGFR2i at 1, 10, or 30 mg/kg once daily for four days. Tumor tissue analysis using Western blotting showed a dramatic suppression of the phosphorylation of FGFR2 downstream effectors in samples derived from mice treated with FGFR2i at 10 or 30 mg/kg and collected 6 h post last dose (Supplementary Fig. S12A). Next, we conducted an efficacy study to evaluate whether inavolisib in combination with the tool FGFR2i inhibitor would improve the therapeutic response in the MFM223 X2.2 xenograft model. Our data showed that single agent treatment with either inavolisib (25 mg/kg) or FGFR2i (10 and 30 mg/kg) daily for 22 days did not result in tumor growth inhibition. In great contrast, treatment with the combination of inavolisib with the FGFR2i triggered a robust tumor regression (Fig 5D, Supplementary Fig. S12A-D). Of note, the treatment regimens were well tolerated, and no treatment-associated body weight losses were observed (Supplementary Fig. S12E).

To explore FGFR2i-inavolisib combination therapy further, we studied whether the emergence of resistance to FGFR2 inhibition could be delayed by a combination treatment with inavolisib. During initial FGFR2i treatment, MFM223 cell line proliferation was strongly inhibited, but eventually, these cells became resistant to the growth-inhibitory effect of the FGFR2i around Day 34 post-treatment initiation, as evidenced by a rebound in proliferation at

this timepoint (Fig. 5E). Similarly, proliferation of MFM223 cells treated with inavolisib was initially inhibited, but this proliferation rebounded after just 11 days (Fig. 5E). In contrast, however, co-treatment with inavolisib and the tool FGFR2i led to sustained inhibition of proliferation in this MFM223 cell line with no apparent rebound up to Day 34 post-treatment start (Fig. 5E). Taken together, these findings suggest that the combination of inavolisib and an FGFR2 inhibitor in *PIK3CA*-mutated and FGFR2-overexpressed cancer could potentially improve response rates to inavolisib and impede acquired resistance to either PI3K or FGFR2 targeted single-agent therapies.

DISCUSSION

The single-agent dose-escalation study of the oral p110α-selective inhibitor, inavolisib (GDC-0077), demonstrated a safety profile consistent with on-target p110α inhibition. The MTD was identified as 9 mg once daily. A linear PK profile supported daily dosing. Anti-tumor activity showed promising preliminary results with an overall response rate of 26% in patients with tumors harboring *PIK3CA* mutations and measurable disease at baseline. Inavolisib treatment led to pharmacodynamic modulation of tumor avidity by FDG-PET and of PI3K/AKT pathway effectors and proliferation in paired tumor biopsies by IHC, and led to decreased *PIK3CA* mutation allele frequency in paired ctDNA samples. Intriguingly, we found *FGFR2* mutations in the liquid biopsies of two patients who received clinical benefit on single-agent inavolisib. Based on this finding, we explored *FGFR2* mutations in a large breast cancer database, and conducted preclinical experiments to decipher the role of *FGFR2* mutations in conjunction with *PIK3CA* mutations.

Based on our findings, we proposed a model (Supplementary Fig. S13) to explain the mechanism whereby tumors that express high levels of FGFR2 (FGFR2-high), in contrast to tumors with low expression of FGFR2, exhibit increased sensitivity to inavolisib (GDC-0077) that is further enhanced when combined with an FGFR2 inhibitor. In FGFR2-dependent tumor models harboring *PIK3CA* hotspot mutations, we demonstrated that FGFR2 is a key regulator of the PI3K pathway by acting on multiple nodes that influence the PI3K signaling cascade. These include HER3, RAS, and with direct binding of FGFR2 to the PI3K regulatory subunit, p85β. Consequently, FGFR2-high cells were highly dependent on PI3K signaling, which in turn increased their susceptibility to PI3K inhibition. We also found that FGFR2 expression

potentiates the degradation of mutated p110α upon inavolisib binding, ultimately leading to an increase in sensitivity to inavolisib.

Previously, we demonstrated that in *ERBB2*-amplified breast cancer cells, HER2 RTK activity plays a key role in regulating mutated p110α degradation upon treatment with inavolisib by recruiting p110α to the cell membrane (14,38). In this study, we established that, in HR+/HER2− breast tumor cells, high FGFR2 RTK activity driven through *FGFR2* alteration (Supplementary Fig. S3, Supplementary Fig. S8) potentiates inavolisib-induced degradation of mutated p110α. Based on the degradation-inducing effects of inavolisib and its observed synergy with FGFR2 inhibitors in *FGFR2*-altered models, we propose that patients with tumors harboring concurrent alterations in *PIK3CA* and *FGFR2* may achieve more complete and durable responses from combined inhibition of the PI3K and other cross-signaling pathways. These results contribute to advancing the conventional precision oncology paradigm based on a single predictive biomarker to more complex matching algorithms based on multiple alterations including in cooperating signaling nodes, and their impact on sensitivity or resistance to specific therapeutic interventions (10,44-47).

Dual blockade of the FGFR2/PI3K signaling axis using non-selective FGFR inhibitors in combination with PI3K inhibitors has previously been proposed based on preclinical cancer models (48,49). However, toxicities associated with these drugs have been a major hurdle for their clinical development, both as single agents and especially as combination therapies. Infigratinib and alpelisib treatment combinations were tested in a Phase 1b clinical trial, NCT01928459, but there was a high rate (71%) of treatment interruptions and dose reductions (49). Hyperphosphatemia-mediated tissue calcification (50) and Grade 3/4 hyperphosphatemia

observed in patients treated with infigratinib (49,51,52), pemigratinib (53,54) and futibatinib (55) have limited the efficacy of FGFR non-selective inhibitors in the clinic. In comparison to other p110α-selective inhibitors (56), the more manageable safety profile of inavolisib may enable combinations with selective RTK inhibitors, including newer and more tolerable FGFR2-selective inhibitors such as RLY-4008 and bemarituzumab (57). Development of additional, mutant-selective PI3K inhibitors can potentially improve the therapeutic index of these combinations further; however, it remains to be seen if lack of inhibition of WT p110α and/or lack of the mutant degradation mechanism represent any potential limitations of these agents.

Our preclinical *in vitro* and *in vivo* experiments suggested that the combination of inavolisib and FGFR2-selective inhibitors prolonged the duration of response and delayed resistance to single-agent therapy. While inavolisib has demonstrated the benefit of a p110α-selective inhibitor as a single agent in patients with *PIK3CA*-mutated, HR+HER2− breast cancer, with an overall response rate of 26% in this population, a clinical benefit rate of 45%, and a PFS rate at 6 months of 37% (95% CI: 15, 59), there may be an opportunity to further improve upon that with combination therapy. In summary, the single-agent dose-escalation study of the oral p110α-selective inhibitor, inavolisib, demonstrated a safety profile consistent with on-target PI3K inhibition, evidence of PI3K pathway inhibition, and anti-tumor activity in a heavily pre-treated advanced cancer patient population; moreover, it illustrated the importance of reverse translational studies from Phase I clinical trial data and refined existing drug development paradigms for cell signaling inhibitors.

ACKNOWLEDGEMENTS

We thank the participants in this study – the patients, and their families. We also convey our appreciation to investigators, staff, and scientists who assisted in the conduct of the clinical trial. Editing and writing assistance was provided by A. Daisy Goodrich (Genentech) and was funded by Genentech. We thank Sophia Maund and Armande Ang Houle for their support in coordinating with the team at Foundation Medicine, Inc.

REFERENCES

1. Millis SZ, Jardim DL, Albacker L, Ross JS, Miller VA, Ali SM, *et al.* Phosphatidylinositol 3-kinase pathway genomic alterations in 60,991 diverse solid tumors informs targeted therapy opportunities. *Cancer* 2019;**125**(7):1185-99 doi 10.1002/cncr.31921.
2. Razavi P, Chang MT, Xu G, Bandlamudi C, Ross DS, Vasan N, *et al.* The Genomic Landscape of Endocrine-Resistant Advanced Breast Cancers. *Cancer Cell* 2018;**34**(3):427-38.e6 doi 10.1016/j.ccell.2018.08.008.
3. Comprehensive molecular portraits of human breast tumours. *Nature* 2012;**490**(7418):61-70 doi 10.1038/nature11412.
4. Kadota M, Sato M, Duncan B, Ooshima A, Yang HH, Diaz-Meyer N, *et al.* Identification of novel gene amplifications in breast cancer and coexistence of gene amplification with an activating mutation of PIK3CA. *Cancer Res* 2009;**69**(18):7357-65 doi 10.1158/0008-5472.Can-09-0064.
5. Madsen RR, Knox RG, Pearce W, Lopez S, Mahler-Araujo B, McGranahan N, *et al.* Oncogenic PIK3CA promotes cellular stemness in an allele dose-dependent manner. *Proc Natl Acad Sci U S A* 2019;**116**(17):8380-9 doi 10.1073/pnas.1821093116.
6. Saito Y, Koya J, Araki M, Kogure Y, Shingaki S, Tabata M, *et al.* Landscape and function of multiple mutations within individual oncogenes. *Nature* 2020;**582**(7810):95-9 doi 10.1038/s41586-020-2175-2.
7. Gorelick AN, Sánchez-Rivera FJ, Cai Y, Bielski CM, Biederstedt E, Jonsson P, *et al.* Phase and context shape the function of composite oncogenic mutations. *Nature* 2020;**582**(7810):100-3 doi 10.1038/s41586-020-2315-8.
8. Hutchinson KE, Chen JW, Savage HM, Stout TJ, Schimmoller F, Cortés J, *et al.* Multiple PIK3CA mutation clonality correlates with outcomes in taselisib + fulvestrant-treated ER+/HER2-, PIK3CA-mutated breast cancers. *Genome Med* 2023;**15**(1):28 doi 10.1186/s13073-023-01181-8.

9. Sivakumar S, Jin DX, Rathod R, Ross J, Cantley LC, Scaltriti M, *et al.* Genetic Heterogeneity and Tissue-specific Patterns of Tumors with Multiple PIK3CA Mutations. *Clin Cancer Res* 2023;**29**(6):1125-36 doi 10.1158/1078-0432.Ccr-22-2270.
10. Vasan N, Razavi P, Johnson JL, Shao H, Shah H, Antoine A, *et al.* Double PIK3CA mutations in cis increase oncogenicity and sensitivity to PI3Kα inhibitors. *Science* 2019;**366**(6466):714-23 doi 10.1126/science.aaw9032.
11. Hochster HS, Hart LL, Ramanathan RK, Childs BH, Hainsworth JD, Cohn AL, *et al.* Safety and efficacy of oxaliplatin and fluoropyrimidine regimens with or without bevacizumab as first-line treatment of metastatic colorectal cancer: results of the TREE Study. *J Clin Oncol* 2008;**26**(21):3523-9 doi 10.1200/jco.2007.15.4138.
12. Drullinsky PR, Hurvitz SA. Mechanistic basis for PI3K inhibitor antitumor activity and adverse reactions in advanced breast cancer. *Breast Cancer Res Treat* 2020;**181**(2):233-48 doi 10.1007/s10549-020-05618-1.
13. Hanan EJ, Braun MG, Heald RA, MacLeod C, Chan C, Clausen S, *et al.* Discovery of GDC-0077 (Inavolisib), a Highly Selective Inhibitor and Degrader of Mutant PI3Kα. *J Med Chem* 2022;**65**(24):16589-621 doi 10.1021/acs.jmedchem.2c01422.
14. Song KW, Edgar KA, Hanan EJ, Hafner M, Oeh J, Merchant M, *et al.* RTK-Dependent Inducible Degradation of Mutant PI3Kα Drives GDC-0077 (Inavolisib) Efficacy. *Cancer Discov* 2022;**12**(1):204-19 doi 10.1158/2159-8290.Cd-21-0072.
15. Turner N, Grose R. Fibroblast growth factor signalling: from development to cancer. *Nat Rev Cancer* 2010;**10**(2):116-29 doi 10.1038/nrc2780.
16. Dienstmann R, Rodon J, Prat A, Perez-Garcia J, Adamo B, Felip E, *et al.* Genomic aberrations in the FGFR pathway: opportunities for targeted therapies in solid tumors. *Ann Oncol* 2014;**25**(3):552-63 doi 10.1093/annonc/mdt419.
17. Babina IS, Turner NC. Advances and challenges in targeting FGFR signalling in cancer. *Nat Rev Cancer* 2017;**17**(5):318-32 doi 10.1038/nrc.2017.8.
18. Zingg D, Bhin J, Yemelyanenko J, Kas SM, Rolfs F, Lutz C, *et al.* Truncated FGFR2 is a clinically actionable oncogene in multiple cancers. *Nature* 2022;**608**(7923):609-17 doi 10.1038/s41586-022-05066-5.
19. Pearson A, Smyth E, Babina IS, Herrera-Abreu MT, Tarazona N, Peckitt C, *et al.* High-Level Clonal FGFR Amplification and Response to FGFR Inhibition in a Translational Clinical Trial. *Cancer Discov* 2016;**6**(8):838-51 doi 10.1158/2159-8290.Cd-15-1246.
20. Clark TA, Chung JH, Kennedy M, Hughes JD, Chennagiri N, Lieber DS, *et al.* Analytical Validation of a Hybrid Capture-Based Next-Generation Sequencing Clinical Assay for Genomic Profiling of Cell-Free Circulating Tumor DNA. *J Mol Diagn* 2018;**20**(5):686-702 doi 10.1016/j.jmoldx.2018.05.004.
21. Frampton GM, Fichtenholtz A, Otto GA, Wang K, Downing SR, He J, *et al.* Development and validation of a clinical cancer genomic profiling test based on massively parallel DNA sequencing. *Nat Biotechnol* 2013;**31**(11):1023-31 doi 10.1038/nbt.2696.
22. Corsello SM, Nagari RT, Spangler RD, Rossen J, Kocak M, Bryan JG, *et al.* Discovering the anti-cancer potential of non-oncology drugs by systematic viability profiling. *Nat Cancer* 2020;**1**(2):235-48 doi 10.1038/s43018-019-0018-6.

23. Hafner M, Niepel M, Chung M, Sorger PK. Growth rate inhibition metrics correct for confounders in measuring sensitivity to cancer drugs. *Nature Methods* 2016;**13**(6):521-7 doi 10.1038/nmeth.3853.
24. Vuong A, Czech B, Gladki A, Hafner M, Scigocki D, Smola J, *et al.* 2024 July 19. gDR: Umbrella package for R packages in the gDR suite. R package version 1.2.0, https://gdrplatform.github.io/gDR/, https://github.com/gdrplatform/gDR. Bioconductor. Accessed 2024 July 19.
25. Bliss CI. The calculation of microbial assays. *Bacteriol Rev* 1956;**20**(4):243-58 doi 10.1128/br.20.4.243-258.1956.
26. Forrest WF, Alicke B, Mayba O, Osinska M, Jakubczak M, Piatkowski P, *et al.* Generalized Additive Mixed Modeling of Longitudinal Tumor Growth Reduces Bias and Improves Decision Making in Translational Oncology. *Cancer Res* 2020;**80**(22):5089-97 doi 10.1158/0008-5472.Can-20-0342.
27. Chen H, Ma J, Li W, Eliseenkova AV, Xu C, Neubert TA, *et al.* A molecular brake in the kinase hinge region regulates the activity of receptor tyrosine kinases. *Mol Cell* 2007;**27**(5):717-30 doi 10.1016/j.molcel.2007.06.028.
28. Hartmaier RJ, Charo J, Fabrizio D, Goldberg ME, Albacker LA, Pao W, *et al.* Genomic analysis of 63,220 tumors reveals insights into tumor uniqueness and targeted cancer immunotherapy strategies. *Genome Med* 2017;**9**(1):16 doi 10.1186/s13073-017-0408-2.
29. Zhao JJ, Liu Z, Wang L, Shin E, Loda MF, Roberts TM. The oncogenic properties of mutant p110alpha and p110beta phosphatidylinositol 3-kinases in human mammary epithelial cells. *Proc Natl Acad Sci U S A* 2005;**102**(51):18443-8 doi 10.1073/pnas.0508988102.
30. Isakoff SJ, Engelman JA, Irie HY, Luo J, Brachmann SM, Pearline RV, *et al.* Breast cancer-associated PIK3CA mutations are oncogenic in mammary epithelial cells. *Cancer Res* 2005;**65**(23):10992-1000 doi 10.1158/0008-5472.Can-05-2612.
31. Kang S, Bader AG, Vogt PK. Phosphatidylinositol 3-kinase mutations identified in human cancer are oncogenic. *Proc Natl Acad Sci U S A* 2005;**102**(3):802-7 doi 10.1073/pnas.0408864102.
32. Sánchez-Guixé M, Hierro C, Jiménez J, Viaplana C, Villacampa G, Monelli E, *et al.* High FGFR1-4 mRNA Expression Levels Correlate with Response to Selective FGFR Inhibitors in Breast Cancer. *Clin Cancer Res* 2022;**28**(1):137-49 doi 10.1158/1078-0432.Ccr-21-1810.
33. Subbiah V, Sahai V, Maglic D, Bruderek K, Touré BB, Zhao S, *et al.* RLY-4008, the First Highly Selective FGFR2 Inhibitor with Activity across FGFR2 Alterations and Resistance Mutations. *Cancer Discov* 2023;**13**(9):2012-31 doi 10.1158/2159-8290.Cd-23-0475.
34. Guagnano V, Kauffmann A, Wöhrle S, Stamm C, Ito M, Barys L, *et al.* FGFR genetic alterations predict for sensitivity to NVP-BGJ398, a selective pan-FGFR inhibitor. *Cancer Discov* 2012;**2**(12):1118-33 doi 10.1158/2159-8290.Cd-12-0210.
35. Ghandi M, Huang FW, Jané-Valbuena J, Kryukov GV, Lo CC, McDonald ER, 3rd, *et al.* Next-generation characterization of the Cancer Cell Line Encyclopedia. *Nature* 2019;**569**(7757):503-8 doi 10.1038/s41586-019-1186-3.

36. Yamamoto H, Shigematsu H, Nomura M, Lockwood WW, Sato M, Okumura N, *et al.* PIK3CA mutations and copy number gains in human lung cancers. *Cancer Res* 2008;**68**(17):6913-21 doi 10.1158/0008-5472.Can-07-5084.
37. Engelman JA, Jänne PA, Mermel C, Pearlberg J, Mukohara T, Fleet C, *et al.* ErbB-3 mediates phosphoinositide 3-kinase activity in gefitinib-sensitive non-small cell lung cancer cell lines. *Proc Natl Acad Sci U S A* 2005;**102**(10):3788-93 doi 10.1073/pnas.0409773102.
38. Olayioye MA, Neve RM, Lane HA, Hynes NE. The ErbB signaling network: receptor heterodimerization in development and cancer. *Embo j* 2000;**19**(13):3159-67 doi 10.1093/emboj/19.13.3159.
39. Yarden Y, Sliwkowski MX. Untangling the ErbB signalling network. *Nat Rev Mol Cell Biol* 2001;**2**(2):127-37 doi 10.1038/35052073.
40. Hynes NE, Lane HA. ERBB receptors and cancer: the complexity of targeted inhibitors. *Nat Rev Cancer* 2005;**5**(5):341-54 doi 10.1038/nrc1609.
41. Eswarakumar VP, Lax I, Schlessinger J. Cellular signaling by fibroblast growth factor receptors. *Cytokine Growth Factor Rev* 2005;**16**(2):139-49 doi 10.1016/j.cytogfr.2005.01.001.
42. Gavine PR, Mooney L, Kilgour E, Thomas AP, Al-Kadhimi K, Beck S, *et al.* AZD4547: an orally bioavailable, potent, and selective inhibitor of the fibroblast growth factor receptor tyrosine kinase family. *Cancer Res* 2012;**72**(8):2045-56 doi 10.1158/0008-5472.Can-11-3034.
43. Zhao G, Li WY, Chen D, Henry JR, Li HY, Chen Z, *et al.* A novel, selective inhibitor of fibroblast growth factor receptors that shows a potent broad spectrum of antitumor activity in several tumor xenograft models. *Mol Cancer Ther* 2011;**10**(11):2200-10 doi 10.1158/1535-7163.Mct-11-0306.
44. Hanker AB, Brown BP, Meiler J, Marín A, Jayanthan HS, Ye D, *et al.* Co-occurring gain-of-function mutations in HER2 and HER3 modulate HER2/HER3 activation, oncogenesis, and HER2 inhibitor sensitivity. *Cancer Cell* 2021;**39**(8):1099-114.e8 doi 10.1016/j.ccell.2021.06.001.
45. Skoulidis F, Heymach JV. Co-occurring genomic alterations in non-small-cell lung cancer biology and therapy. *Nat Rev Cancer* 2019;**19**(9):495-509 doi 10.1038/s41568-019-0179-8.
46. Negrao MV, Araujo HA, Lamberti G, Cooper AJ, Akhave NS, Zhou T, *et al.* Comutations and KRASG12C Inhibitor Efficacy in Advanced NSCLC. *Cancer Discov* 2023;**13**(7):1556-71 doi 10.1158/2159-8290.Cd-22-1420.
47. Varkaris A, Fece de la Cruz F, Martin EE, Norden BL, Chevalier N, Kehlmann AM, *et al.* Allosteric PI3Kα Inhibition Overcomes On-target Resistance to Orthosteric Inhibitors Mediated by Secondary PIK3CA Mutations. *Cancer Discov* 2024;**14**(2):227-39 doi 10.1158/2159-8290.Cd-23-0704.
48. Packer LM, Geng X, Bonazzi VF, Ju RJ, Mahon CE, Cummings MC, *et al.* PI3K Inhibitors Synergize with FGFR Inhibitors to Enhance Antitumor Responses in FGFR2(mutant) Endometrial Cancers. *Mol Cancer Ther* 2017;**16**(4):637-48 doi 10.1158/1535-7163.Mct-16-0415.

49. Hyman DM, Tran B, Paz-Ares L, Machiels JP, Schellens JH, Bedard PL, *et al.* Combined PIK3CA and FGFR Inhibition With Alpelisib and Infigratinib in Patients With PIK3CA-Mutant Solid Tumors, With or Without FGFR Alterations. *JCO Precis Oncol* 2019;**3**:1-13 doi 10.1200/po.19.00221.
50. Brown AP, Courtney CL, King LM, Groom SC, Graziano MJ. Cartilage dysplasia and tissue mineralization in the rat following administration of a FGF receptor tyrosine kinase inhibitor. *Toxicol Pathol* 2005;**33**(4):449-55 doi 10.1080/01926230590961845.
51. Nogova L, Sequist LV, Perez Garcia JM, Andre F, Delord JP, Hidalgo M, *et al.* Evaluation of BGJ398, a Fibroblast Growth Factor Receptor 1-3 Kinase Inhibitor, in Patients With Advanced Solid Tumors Harboring Genetic Alterations in Fibroblast Growth Factor Receptors: Results of a Global Phase I, Dose-Escalation and Dose-Expansion Study. *J Clin Oncol* 2017;**35**(2):157-65 doi 10.1200/jco.2016.67.2048.
52. Javle M, Lowery M, Shroff RT, Weiss KH, Springfeld C, Borad MJ, *et al.* Phase II Study of BGJ398 in Patients With FGFR-Altered Advanced Cholangiocarcinoma. *J Clin Oncol* 2018;**36**(3):276-82 doi 10.1200/jco.2017.75.5009.
53. Abou-Alfa GK, Sahai V, Hollebecque A, Vaccaro G, Melisi D, Al-Rajabi R, *et al.* Pemigatinib for previously treated, locally advanced or metastatic cholangiocarcinoma: a multicentre, open-label, phase 2 study. *Lancet Oncol* 2020;**21**(5):671-84 doi 10.1016/s1470-2045(20)30109-1.
54. Subbiah V, Iannotti NO, Gutierrez M, Smith DC, Féliz L, Lihou CF, *et al.* FIGHT-101, a first-in-human study of potent and selective FGFR 1-3 inhibitor pemigatinib in pan-cancer patients with FGF/FGFR alterations and advanced malignancies. *Ann Oncol* 2022;**33**(5):522-33 doi 10.1016/j.annonc.2022.02.001.
55. Goyal L, Meric-Bernstam F, Hollebecque A, Valle JW, Morizane C, Karasic TB, *et al.* Futibatinib for FGFR2-Rearranged Intrahepatic Cholangiocarcinoma. *N Engl J Med* 2023;**388**(3):228-39 doi 10.1056/NEJMoa2206834.
56. Juric D, Rodon J, Tabernero J, Janku F, Burris HA, Schellens JHM, *et al.* Phosphatidylinositol 3-Kinase α-Selective Inhibition With Alpelisib (BYL719) in PIK3CA-Altered Solid Tumors: Results From the First-in-Human Study. *J Clin Oncol* 2018;**36**(13):1291-9 doi 10.1200/jco.2017.72.7107.
57. Xiang H, Chan AG, Ahene A, Bellovin DI, Deng R, Hsu AW, *et al.* Preclinical characterization of bemarituzumab, an anti-FGFR2b antibody for the treatment of cancer. *MAbs* 2021;**13**(1):1981202 doi 10.1080/19420862.2021.1981202.

Table 1. Demographics and baseline characteristics

	Inavolisib dose cohort			All cohorts
	6 mg	**9 mg**	**12 mg**	
	***N*=7**	***N*=9**	***N*=4**	***N*=20**
Age				
Median	64	69	61	65
Range	56–73	55–73	41–77	41–77
Sex, (%)				
Male	0	0	1 (25)	1 (5)
Female	7 (100)	9 (100)	3 (75)	19 (95
Race, *n* (%)				
Black or African American	0	0	1 (25)	1 (5)
White	4 (57)	8 (89)	2 (50)	14 (70)
Unknown	3 (43)	1 (11)	1 (25)	5 (25)
ECOG performance status at baseline				
0	3 (43)	5 (56)	3 (75)	11 (55)
1	4 (57)	4 (44)	1 (25)	9 (45)
Weight at baseline (kg)				
Median	72	61	84	65
Range	57–94	55–85	68–111	55–111
Body mass index (BMI) at baseline, *n* (%)				
≥30 kg/m^2	3 (43)	0	2 (50)	5 (25)
Prior lines of therapy in metastatic setting				
Median	3	3	4	3
Range	2–10	1–10	2–5	1–10
Prior therapies				
Chemotherapy	7 (100)	8 (89)	4 (100)	19 (95)
CDK4/6 inhibitor	6 (86)	9 (100)	3 (75)	18 (90)
Aromatase inhibitor	7 (100)	9 (100)	3 (75)	19 (95)
SERD	5 (71)	6 (67)	2 (50)	13 (65)
Fulvestrant	5 (71)	6 (67)	2 (50)	13 (65)

Table 2. Adverse events related to inavolisib

MedDRA Preferred Term	All Grade Related AE (*N*=20)	Grade 3-5 Related AE (*N*=20)
Total number of patients with at least one AE, *n* (%)	19 (95)	8 (40)
Hyperglycemia	14 (70)	4 (20)
Diarrhea	9 (45)	0
Decreased appetite	4 (20)	0
Stomatitis (grouped term) *	4 (20)	0
Vomiting	4 (20)	0
Fatigue	3 (15)	1 (5)
Nausea	3 (15)	1 (5)
Weight decreased	3 (15)	1 (5)
Alopecia	3 (15)	0
Asthenia	2 (10)	1 (5)
Lymphopenia	2 (10)	1 (5)
Constipation	2 (10)	0
Dysgeusia	2 (10)	0
Flatulence	2 (10)	0
Headache	2 (10)	0
Hyponatremia	2 (10)	0
Taste disorder	2 (10)	0
Thrombocytopenia	2 (10)	0
Vision blurred	2 (10)	0

* Stomatitis (grouped terms) = stomatitis, mucosal inflammation, & palatal ulcer

Figure 1. Clinical profile of inavolisib as a single agent. A, Twenty patients were enrolled in an open label, Phase 1, dose escalation study to investigate once-daily inavolisib dosing. **B**, The mean plasma concentration versus time profiles for single and multiple dose oral inavolisib demonstrated a linear profile and supported daily dosing. **C**, Proliferative and PI3K pathway activity were decreased in a majority of paired tumor samples as assessed by immunohistochemistry for Ki67, phosphorylated AKT, and phosphorylated S6. **D**, FDG-PET scans at baseline and after 2 weeks of daily inavolisib showed metabolic responses at all dose levels evaluated. **E**, Decreased *PIK3CA* mutation allele frequency was observed over time in the majority of paired specimens from patients who experienced a partial response. **F**, Twenty patients were evaluated for efficacy, of whom 19 had measurable disease; the best overall response rate was 26%, confirmed overall response rate was 21% among the 19 patients with measurable disease, and the clinical benefit rate was 45% among all 20 patients.

Figure 2. *FGFR2* expression is associated with inavolisib sensitivity in patients with *PIK3CA*-mutated breast cancer. **A**, *FGFR2* mutations were identified in baseline liquid biopsies of patients who experienced clinical benefit from inavolisib. FGFR2 N549K mutations are highlighted with a cross, and identified mutations in *PTEN* and *AKT1* are also noted. **B**, Lollipop plot of the landscape of known and likely *FGFR2* alterations across 49,834 breast tumors that underwent comprehensive genomic profiling (CGP). **C**, Volcano plot illustrating the co-occurrence (purple) or mutual exclusivity (gray) of *FGFR2* SV with alterations in other CGP-baited genes across the cohort of breast tumor samples shown in **b**. **D**, Inavolisib area under the sigmoid-fit concentration-response curve (AUC) values across 662 PRISM cancer cell lines. Inavolisib AUC values of *PIK3CA* hotspot mutant versus *PIK3CA* non-hotspot mutant (other) or wildtype (WT) and *FGFR2* hotspot altered versus *FGFR2* non-hotspot altered (other) or WT were compared. *PIK3CA*-WT/other and *FGFR2*-WT/other, *n*=581; *PIK3CA*-hotspot and *FGFR2*-WT/other, *n*=78; *PIK3CA*-WT/other and *FGFR2*-hotpsot, *n*=7; *PIK3CA*-hotspot and *FGFR2*-hotpsot, *n*=7. **E**, Correlation of FGFR2 expression versus inavolisib AUC values across PRISM cell lines (*n*=662). **F**, Comparison of inavolisib AUC values of *PIK3CA*-hotspot versus *PIK3CA*-WT/other and top-33.3% versus bottom-33.3% *FGFR2* expressing PRISM cell lines. *PIK3CA*-WT/other and *FGFR2*-bottom-33.3%, *n*=213; *PIK3CA*-hotspot and *FGFR2*-bottom-33.3%, *n*=8; *PIK3CA*-WT/other and *FGFR2*-top-33.3%, *n*=173; *PIK3CA*-hotspot and *FGFR2*-top-33.3%, *n*=48. **G**, Western blot of cell lysates (*n*=16) with *FGFR2* alterations blotted for FGFR1/2/3/4 and actin. Blue labels indicate cell lines with visually detectable FGFR2 expression, and red labels indicate cell lines with non-visually detectable FGFR2 protein expression by Western blot. Representative results from experiments (*n*=2). **H**, Correlations of

FGFR1-4 expression versus relative cell viability values after specific targeting of *FGFR1*, *2*, *3*, or *4* using siRNAs, as assessed by quantifying ATP levels 5 days post-transfection, across FGFR2-high (*n*=6) and FGFR2-low (*n*=9) cell lines. Representative results from experiments (*n*=2). **I**, Comparison of relative cell viability values in FGFR2-high (*n*=6) versus FGFR2-low (*n*=9) cell lines following 5-day FGFR2 silencing. Representative results from experiments (*n*=2). **J**, (Upper panel) biochemical enzyme activity of FGFR2i. (Bottom panel) comparison of half-maximal growth inhibition concentration (GR50) values for a tool FGFR2 inhibitor (FGFRi) in FGFR2-high (*n*=6) versus FGFR2-low (*n*=9) cell lines. Data in (**D, F, I, J**) are represented as median (center line) ± interquartile range (IQR, 25th to 75th percentile, box) and ± full range (minimum to maximum, whiskers). *P* values were calculated with one-tailed one-way ANOVA and FDR multiple testing corrections using the two-stage step-up method from Benjamini, Krieger, and Yekutieli (**D, F**), two-tailed *t*-transformations of Pearson's *R* correlation coefficients (**E, H**), two-tailed unpaired Student's *t*-tests (**I**), or Wilcoxon's ranksum test (**J**).

Figure 3. High FGFR2 expression is associated with inavolisib sensitivity.

A, Oncoplot showing *FGFR2* alterations and transcript expression (log_2[TPM, transcripts per million]) in *PIK3CA* hotspot mutant (E542K, E545K, H1047R/L) cell lines (*n*=29). FGFR2 protein expression categories (high, low), as assessed by western blot in Supplementary Fig. S6B, concurrent alterations affecting *PIK3CA*, *ERBB2*, and/or *RAS*, and inavolisib GR50 values as assessed by quantifying ATP at 5 days post treatment, are also indicated. **B**, Comparison of inavolisib GR50 values in *PIK3CA* mutant FGFR2-high (*n*=12) versus FGFR2-low cell lines that contain secondary *PIK3CA* alterations (SV, *n*=2; amplification, *n*=1), high p-HER2 levels (*n*=6), or RAS alterations (*KRAS* amplification, *n*=2; *RASA1* loss-of-function, *n*=1) versus FGFR2-low cell lines that contain none of these alterations (*n*=5). Data are represented as median (center line) ± IQR (25th to 75th percentile, box) and ± full range (minimum to maximum, whiskers). *P* value was calculated using a Wilcoxon's rank sum test. Representative results from experiments (*n*=2).

Figure 4. Inavolisib sensitivity depends on high FGFR2 expression.

A, Legend related to panels in b-i. **B**, Cell lines were treated with 0.03 μM of an FGFR2 inhibitor (FGFR2i) or 2 μM lapatinib for 1 h followed by immunoblotting with the antibodies indicated at left. Representative results from experiments (*n*=2). **C**, Cell lines were treated with inavolisib or the FGFR2i at various concentrations for 1 h. Cell lysates were immunoprecipitated with an antibody against p85β, followed by immunoblotting with the antibodies indicated at left. Representative results from experiments (*n*=2) **D**, Following RAS-GTP pull-down, cell lines were treated with the FGFR2i or lapatinib for different durations and immunoblotted with the antibodies indicated at left. Representative results from experiments (*n*=2) **E**, Cell lysates from cells treated with inavolisib alone or in combination with FGFR2i or lapatinib for 4 h were immunoprecipitated with RAS antibody and blotted with p110α antibody. **F**, Mechanistic model of the effects of FGFR2 and HER2 inhibition on HER3 and RAS activity. FGFR2-high expressing cell lines induced PI3K signaling through both HER3 and WT RAS activity (*top*) compared to HER2-induced PI3K signaling through HER3 but not RAS activity (*bottom*). **G**, FGFR2-high expressing cell lines, MFM223 and SUM52PE, were treated with inavolisib, FGFR2i, or lapatinib for 1 h. Membrane fractions were analyzed by reciprocal co-immunoprecipitation with one another using HER3 or FGFR2 antibody and WB with FGFR2, HER3, RAS, and p85β antibody. Representative results from experiments (*n*=2). **H**, SUM52PE, MFM223, and MFE280 cells were treated with inavolisib single-agent or in combination with FGFR2i or lapatinib for 6 h. Ubiquitinated proteins were pulled down from the membrane fraction with TUBE1 reagent and blotted with p110α antibody. Representative results from experiments (*n*=2). **I**, Western blots of the inhibitor response in PI3K signaling (pHER3 and

pAKT) in *PIK3CA* mutant MFM223 and *PIK3CA* WT SUM52PE; cell lines were treated with 0.5 μM inavolisib or 1 μM alpelisib for different durations. Representative results from experiments (*n*=2). **J**, Ratio of inavolisib and alpelisib GR50 values in FGFR2-high (*n*=12) versus FGFR2-low (*n*=9) expressing cell lines harboring *PIK3CA* mutations, as assessed in a 5-day viability assay. Data are represented as median (center line) ± IQR (25th to 75th percentile, box) and ± full range (minimum to maximum, whiskers). *P* value was calculated using Wilcoxon's rank sum test. Representative results from experiments (*n*=2).

Figure 5. Inavolisib and FGFR2 inhibitor combination produces a synergistic effect in FGFR2-high cell lines. **A**, Representative dose-response curves of SUM52PE, AN3CA2, and HEC151 cell lines transfected with *FGFR1-4*-selective siRNA and treated at different concentrations of inavolisib for 18 h. Error bars represent the standard deviation of triplicates. Representative results from experiments (*n*=2). **B**, Drug combination effect on cell lines (*n*=13) treated with inavolisib and FGFR2 inhibitor (FGFR2i) as a two-way 10 × 8 serial dilution matrix to calculate the Bliss excess scores for each cell line. Representative results from experiments *(n*=2). **C**, SUM52PE and AN3CA cells were transfected with *FGFR1-4*-selective siRNA or vehicle control and 0.4 μM, and 2 μM inavolisib for 18 h. Cells were harvested and immunoblotted with antibodies indicated on the left. **D**, Fitted tumor volumes of MFM223 X2.2 (Breast, p110α H1047R, *FGFR2* amplified) xenograft model treated daily for 22 days with inavolisib, FGFR2i, or combination treatment. **E**, Cells treated with FGFR2i or inavolisib alone or in combination with both inhibitors imaged over time using IncuCyte.

Author Contributions

1. Conceived, designed and planned the study.
2. Collected data.
3. Provided study oversight.
4. Performed the statistical analysis.
5. Prepared the first draft of the manuscript.
6. interpreted the results
7. Provided critical review and revision of the drafts, and approved the decision to submit for publication.

1	Alice Wong	1, 6, 7
2	Andrea Varga	2, 6, 7
3	Andrés Cervantes	2, 6, 7
4	Antoine Italiano	2, 6, 7
5	Anwesha Dey	1, 3, 5, 6, 7
6	Cristina Saura	3, 6, 7
7	Daniel Zingg	4, 6, 7
8	Danilo Maddalo	1, 3, 6, 7
9	Dejan Juric	2, 6, 7
10	Erika Hamilton	2, 6, 7
11	Ethan S. Sokol	2, 6, 7
12	Eva Lin	2, 6, 7
13	Ian E. Krop	2, 6, 7
14	Jeffery T. Lau	2, 6, 7
15	Jennifer A. Roth	2, 4, 6
16	Jennifer L. Schutzman	1, 3, 6, 7
17	Jill Fredrickson	1, 2, 3, 5, 6
18	Junko Aimi	1, 2, 3, 7
19	Katherine E. Hutchinson	1, 2, 3, 4, 5, 6, 7
20	Kevin Kalinsky	1, 2, 3, 6, 7
21	Komal L Jhaveri	2, 6, 7
22	Kyung Song	1, 2, 4, 5, 6, 7
23	Mafalda Oliveira	2, 6, 7
24	Marc Hafner	2, 4, 6
25	Matthew G. Rees	2, 4, 6
26	Melissa K. Accordino	2, 6, 7
27	Melissa M. Ronan	2, 4, 6
28	Michael S. Hwang	1, 6, 7
29	Nicholas C. Turner	2, 6, 7
30	Nicole M. Sodir	1, 3, 6, 7

31	Noopur Shankar	3, 6, 7
32	Peter Schmid	2, 6, 7
33	Philippe L. Bedard	2, 6, 7
34	Radia M. Johnson	1, 2, 4, 5, 6, 7
35	Robert L. Yauch	3, 6, 7
36	Scott Martin	2, 6, 7
37	Sravanthi Cheeti	4, 6, 7
38	Stephanie Hilz	4, 6, 7
39	Stephanie Royer-Joo	1, 3, 6, 7
40	Steven Gendreau	3, 6, 7
41	Trang Pham	3, 5
42	Ubong Peters	3, 5, 6, 7
43	Valentina Gambardella	2, 6, 7
44	Yanling Jin	4, 6, 7
45	Zachary J.Whitfield	2, 6, 7
46	Zheng Kuang	4, 6, 7

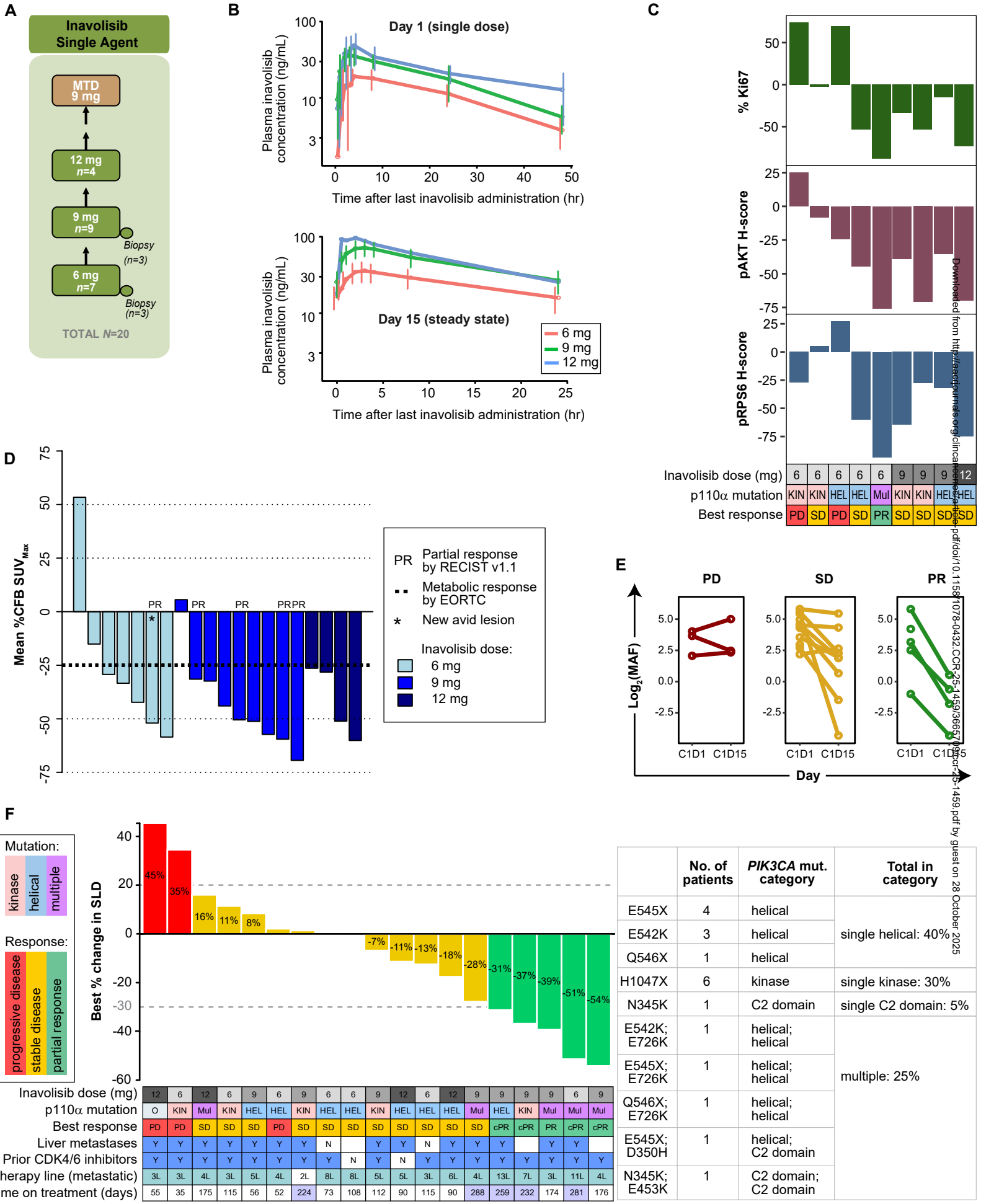

	No. of patients	*PIK3CA* mut. category	Total in category
E545X	4	helical	single helical: 40%
E542K	3	helical	
Q546X	1	helical	
H1047X	6	kinase	single kinase: 30%
N345K	1	C2 domain	single C2 domain: 5%
E542K; E726K	1	helical; helical	multiple: 25%
E545X; E726K	1	helical; helical	
Q546X; E726K	1	helical; helical	
E545X; D350H	1	helical; C2 domain	
N345K; E453K	1	C2 domain; C2 domain	

FIGURE 1

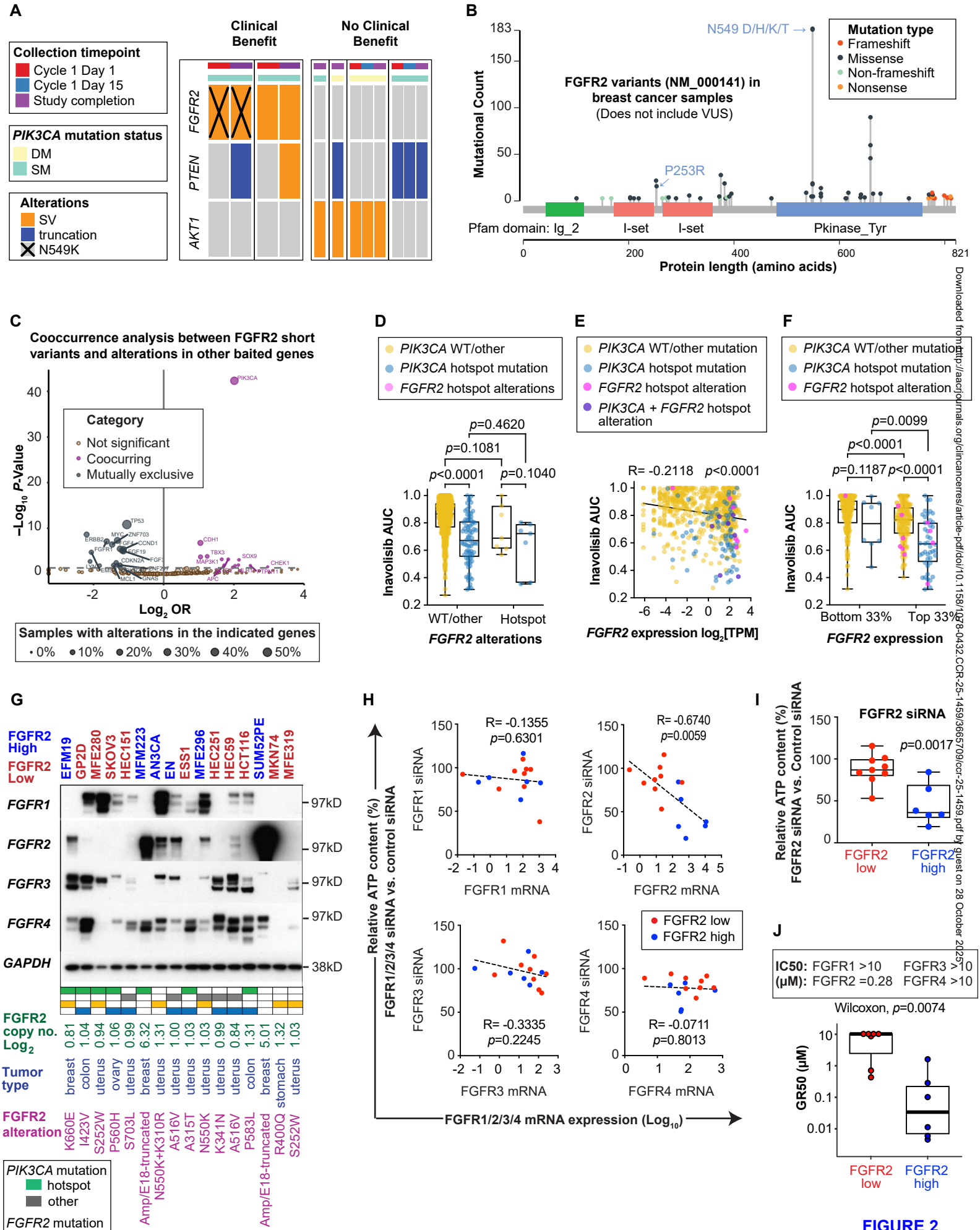

FIGURE 2

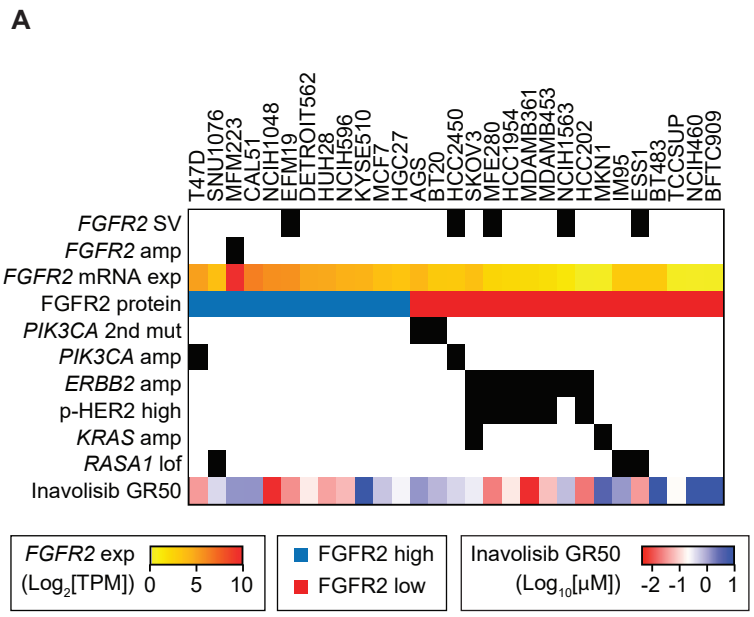

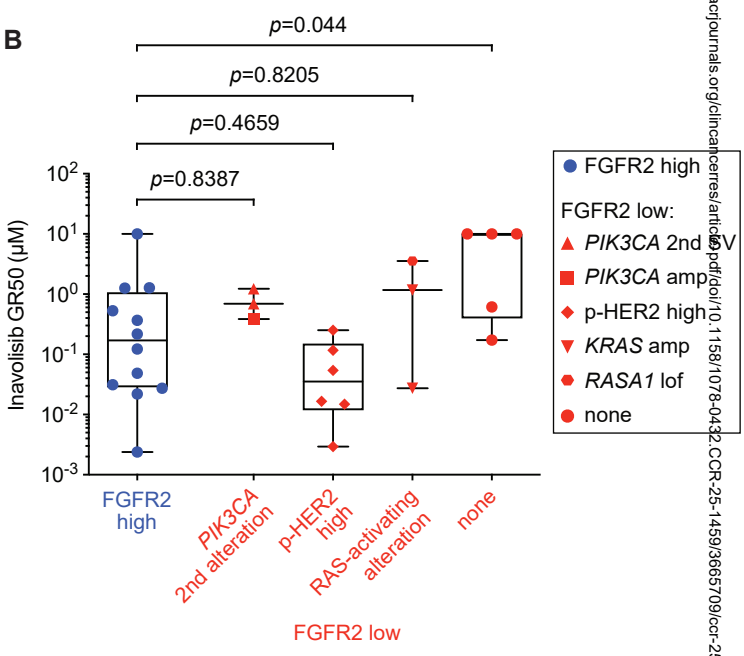

FIGURE 3

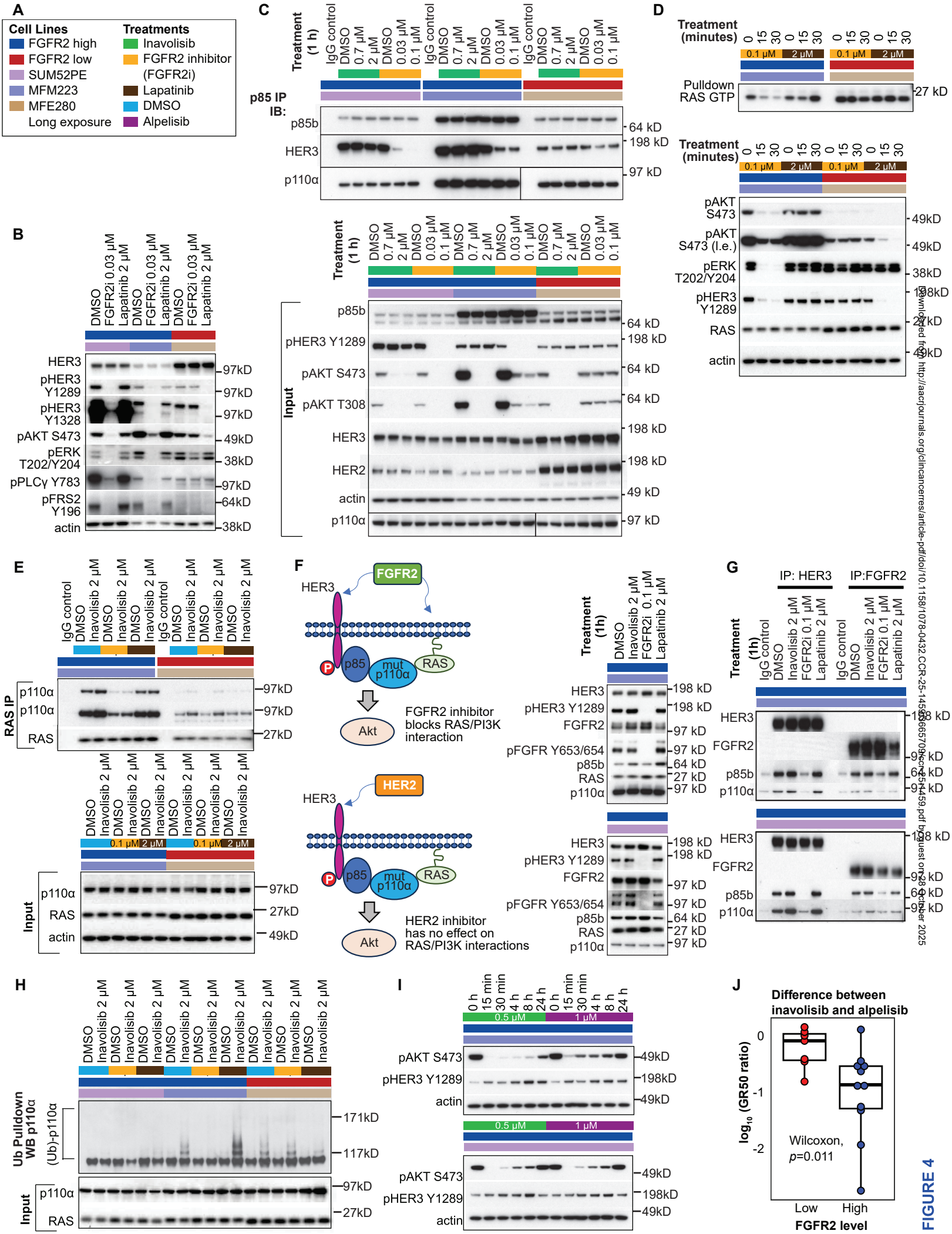

FIGURE 4

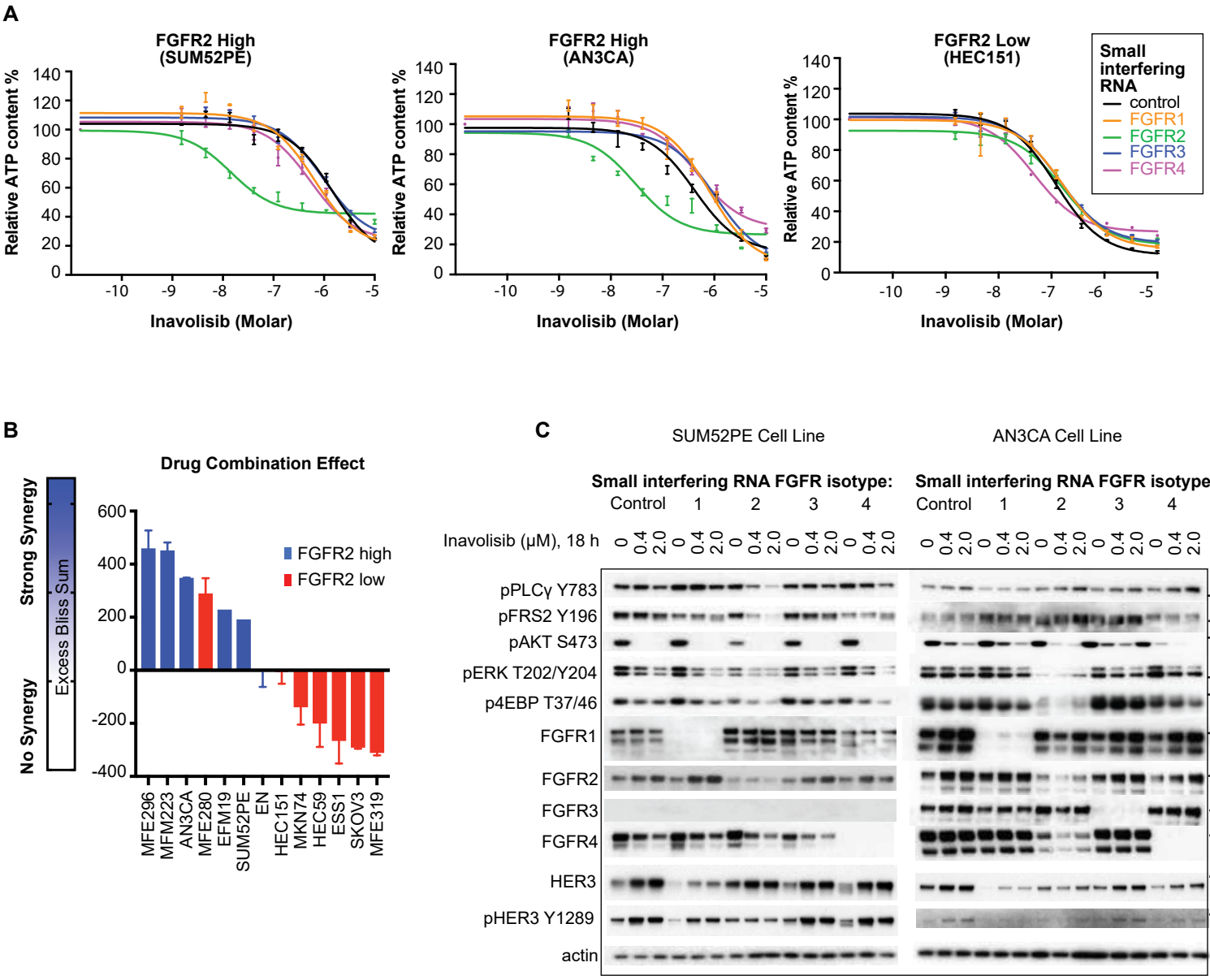

FIGURE 5